Search for associated production of a single top-quark and a Z boson in a dilepton final state with the ATLAS detector

Dorothee Sophie Wohlleben

Masterarbeit in Physik
angefertigt im Physikalischen Institut

vorgelegt der
Mathematisch-Naturwissenschaftlichen Fakultät
der
Rheinischen Friedrich-Wilhelms-Universität
Bonn

October 2017

I hereby declare that this thesis was formulated by myself and that no sources or tools other than those cited were used.

Bonn, ...
Date Signature

1. Gutachter: Prof. Dr. Ian C. Brock
2. Gutachter: Priv.-Doz. Dr. Markus Cristinziani

Contents

CHAPTER 1

Introduction

Since the beginnings of the human race, people have struggled to understand both themselves and the universe in which they live. Attempts to gain a better understanding were and are still being made in many different directions, be they history, philosophy or religion. One very basic question out of many is, what the universe is actually made of? What is matter and why does it behave as it does? In an attempt to, if not understand then at least describe physical observations, many theoretical models were made and tested. One such model is the Standard Model, which attempts to describe the smallest constituents of matter predicted at this point as well as their interactions. However, even though the model is extensive, it does not explain all observed effects. Accordingly the Standard Model is checked on many different levels to find indications for possible errors and to confirm at least parts of it with relative certainty. It has been the objective of many experimental particle physicists for the past fifty or so years to find the predicted particles, cross check their behaviour and search for additional, not expected occurrences.

With the Higgs boson being discovered in 2012 at the Large Hadron Collider at CERN, the last particle predicted by the Standard Model was confirmed. However, the cross checks for the behaviour of the different particles are far from finished. One particular particle of interest is the top quark, which with a mass of roughly 173 GeV is the heaviest one in the Standard Model. It is of special interest since, due to a very short lifetime, it decays before forming bound states. This allows for the spin information to be carried on to its decay products. There are several different possible production modes. While the dominant production modes have already been studied extensively, those with lower cross-sections are a topic of current research. Due to their low cross-sections they are called rare production modes. Two such production modes, which are currently being researched are single top-quark production in association with a Z boson and the single top production in association with a Higgs boson. The associated production of a top quark with a Z-boson (tZq) is sensitive to two different couplings: the tZ coupling as well as the WWZ coupling. In addition, at the beginning of this thesis the production had not yet been observed. The theory prediction of its NLO cross-section is $800\,\text{fb}^{+6.1}_{-7.4}\%$ [1]. Finally the Standard Model production of tZq is of interest as a background to beyond Standard Model searches such as flavour changing neutral currents. It is also a background for the single top-quark production in association with a Higgs boson. The cross-section of the single top-quark production in association with a Higgs boson (tHq) is very dependent on the Higgs couplings. If they differ even slightly from those predicted by the Standard Model, the cross-section measurement will reflect this.

Based on the decay of the Z-boson and the top quark, there are in total four different possible channels for the final states of tZq: one containing only hadrons, one containing a single lepton, one with two leptons and finally one containing three leptons. For the channel with three leptons, the so called "trilepton" channel, an inclusive cross-section measurement was recently performed giving a cross-section

of $\sigma_{tZq} = (600 \pm 170\,(\text{stat.}) \pm 140\,(\text{sys.}))\,\text{fb}$ with a significance of $4.2\,\sigma$.

This thesis focuses on the dilepton channel. After introducing the Standard Model and top quark related physics in chapter 2, the ATLAS detector is described in chapter 3. The ATLAS detector is a detector at the Large Hadron Collider, which is used to gather the data analysed in this thesis. In addition to the measured data, Monte Carlo simulated events are used in the analysis. Details of the simulated samples are introduced in chapter 4 as well as the method of object reconstruction in ATLAS. In order to gain the best results possible, the signal and background separation is optimised using a Neural Network. which is described in chapter 5. Finally, in chapter 6 an upper limit on cross section is computed at 95 % confidence level. Different systematic uncertainties are included, which will also be introduced in chapter 6. Further studies done concerning possible improvements and future directions were included in appendix A. The results are summarised in the last chapter.

CHAPTER 2

Theoretical concepts

This chapter offers a short introduction into particle physics with special emphasis on top-quark physics. The general description of particle physics in section 2.1 is summarised from Ref. [2] and Ref. [3]. The details concerning top-quark physics in section 2.2 are taken from Ref. [4] and Ref. [5].

2.1 Introduction to particle physics

Particle physics considers the physics of the smallest irreducible particles and their interactions. The currently accepted model of particle physics is the Standard Model (SM). The model describes the elementary particles and their forces. Elementary particles are those, which have no substructure. The forces are described by the exchange of such elementary particles. There are in total four fundamental forces: gravity, strong, weak and electromagnetic. However, gravity is not considered in the Standard Model as its effects on elementary particles are negligible.

The electormagnetic force is already quite well known due to the interaction between electrons and nuclei. While electrons have a negative electric charge, protons have a positive one. The interaction particle for the electromagnetic force is the photon. However neither protons nor neutrons are elementary particles, rather they consist of even smaller particles. An additional force is needed in order to explain why these smaller particles form – for example – protons or neutrons. This force is called the strong force and it's interaction particle is the gluon. The final, so called weak force, is as the name already states weaker than the strong and electromagnetic force at the currently produced energy levels. It can for example be observed in the β-decay, which is one possible decay of nuclei. The interaction particles of the weak force are the Z and the $W^{\pm}$ bosons.

In addition to the particles used to describe the forces, which are called bosons, the Standard Model contains two further particle groups: leptons and quarks. Six quarks, six leptons and their corresponding antiparticles have been discovered so far and there is strong experimental evidence that no further exist. The difference between these two types of elementary particles is the force with which they interact. Only if a particle carries the charge which is associated with the force can it interact with the force. Which charges a particle carries depends on the particle type. The most commonly known of these charges is the electric charge. The electron, a lepton, carries a negative electric charge of $-1e$. The muon and the tau, two additional leptons, also carry a negative electric charge of $-1e$, however their masses differ (see table 2.1). All three particles have a corresponding antiparticle with the same mass, but a positive electric charge of $+1e$. In addition to these, there are three corresponding neutrinos: the electron neutrino, the muon neutrino and the tau neutrino. It is a topic of current research, if there are antineutrinos, or if neutrinos are their own antiparticles. In contrast to the electron, muon and tau, the neutrinos do not carry

Leptons			Quarks		
Name	Charge/e	Mass/GeV	Name	Charge/e	Mass/GeV
electron	-1	0.0005	down	$-1/3$	0.005
electron neutrino	0	$< 2 \cdot 10^{-9}$	up	$+2/3$	0.002
muon	-1	0.106	strange	$-1/3$	0.1
muon neutrino	0	$< 2 \cdot 10^{-9}$	charm	$+2/3$	1.3
tau	-1	1.78	bottom	$-1/3$	~4.5
tau neutrino	0	$< 2 \cdot 10^{-9}$	top	$+2/3$	173

Table 2.1: Properties of leptons and quarks in the Standard Model [6].

an electric charge. Accordingly neutrinos can not interact electromagnetically. They can however interact weakly. All known elementary particles can interact weakly.

The second large group of elementary particles are the quarks. There are in total 6 quarks and 6 antiquarks, which have the same mass, but the exact opposite charge. The quarks can have an electric charge of $-1/3e$ or $+2/3e$. The antiquarks can have an electric charge of $1/3e$ or $-2/3e$. In addition to the electric charge, the quarks also carry the so called "colour charge" and the antiquarks an "anticolour charge". This is the corresponding charge for the strong force. The possible charges are "red", "blue" and "green" with the corresponding anticharges of "antired", "antiblue" and "antigreen". Leptons do not carry colour charge and accordingly cannot interact strongly. Due to the nature of the strong force quarks can never exist as free particles for a time-scale longer than that of strong interactions, which is at about 10×10^{-23} s. Instead they form hadrons, which consist of several quarks. This effect is called "confinement". Even though quarks carry colour charge, particles which exist over longer periods of time must be colour neutral. This can be reached by either combining all three colours or all three anticolours, or by combining one colour with its corresponding anticolour. If a colour and anticolour are combined the resulting particle is called a meson. Protons and neutrons consist of three valence quarks and additional sea quarks. Particles of this kind are called baryons. The different quark contents also lead to different spins. The spin is an intrinsic form of angular momentum. It can take values of 0, $\pm\frac{1}{2}$ and ± 1, as well as combinations of them. Each elementary particle has an assigned spin. All mesons have an integer spin, while all baryons have a half-integer spin. Particles with an integer spin are called bosons, while particles with a half-integer spin are called fermions. The interaction particles are all bosons, while all leptons and quarks are fermions. Quarks have masses between 0.002 GeV and 173 GeV (see table 2.1). The unit commonly used in particle physics is eV with 1 eV being equivalent to 1.6×10^{-19} J. Strictly speaking the unit of mass would have to be eV c^{-2}, but in particle physics the so called "natural units" are commonly used for which the Plank constant $\hbar$ and the speed of light c are set equal to one.

2.1.1 Quantum Field Theory and the Higgs boson

There are certain rules according to which different particles can interact with the bosons. Not only are different charges necessary to make interactions possible, there are several additional properties of the different interactions, which must be considered. The properties of each force are described by an associated Quantum Field Theory (QFT). In the case of the electromagnetic interaction this is done by the Quantum Electrodynamics (QED), which has a U(1) gauge group symmetry. For the weak interaction the theory is called Quantum Flavourdynamics, which has a SU(2) gauge group symmetry. Finally the strong interaction is described by the Quantum Chromodynamics (QCD), which has a SU(3) group symmetry. The weak and electromagnetic force are these days commonly considered as two different manifestations of a single electroweak force. The theory describing this unification of the two forces

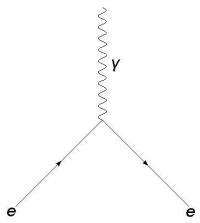

Figure 2.1: Basic QED vertex of electron interacting with a photon.

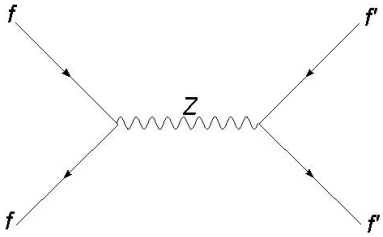

Figure 2.2: A fermion and antifermion annihilating to a Z boson and creating a different fermion pair.

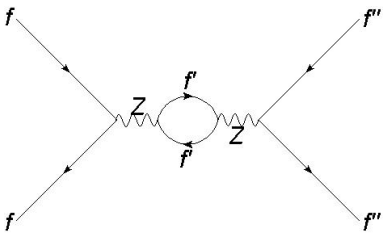

Figure 2.3: A next-to-leading order (NLO) QED diagram with one loop.

is the Glashow-Weinberg-Salam Theory (GWS). It proposes four different massless mediators out of which three ($W^{\pm}$, Z) gain mass due to the Higgs mechanism. The Higgs particle was discovered at the Large Hadron Collider (LHC) in 2012, which is the particle corresponding to the Higgs mechanism [7]. Different from the other bosons, which are spin 1 particles, the Higgs boson is a spin 0 scalar particle. The masses of the $W^{\pm}$-, Z- and the Higgs bosons are all in the order of 100 GeV. A unification of the GWS and QCD is called a Grand Unified Theory (GUT).

2.1.2 Interaction processes

In order to visualise the different quantum field theories, Feynman developed a graphic representation for them: the Feynman diagrams. Using these graphs and the corresponding rules it is possible to calculate the cross-section (see section 2.1.3) of the described process. The most straightforward Feynman diagrams consist of a single vertex. Either one particle decays into two, or two particles annihilate to a single one. For example in QED they consist of two fermions and one photon (see figure 2.1). All other Feynman diagrams can be reduced to combinations of such vertices. Each of the vertices associates with the square root of a coupling constant. The coupling constants are directly related to the interaction type. They are energy dependent. However in the case of the electromagnetic interaction it is almost constant for the relevant energy regions. Accordingly it can be approximated as $\alpha_{\text{em}} \approx 1/137$ [6]. In the case of the strong interaction such an approximation is not possible. It is for the relevant energy regions of the order of 1. More information on the coupling constants can be found in Ref. [2].

For this thesis the convention of the time moving from the left to the right is used. For more information on the conventions used see Ref. [3]. In the case of figure 2.1 one incoming electron interacts with a photon. The outgoing particle is once again an electron, but due to the interaction with the photon it has different properties. For example the energy of the electron will have changed. One of the most commonly considered graphs consists of two incoming and two outgoing particles which interact through one of the bosons (see figure 2.2). The diagrams are sorted into three main groups, the s-, t- and u-channel diagrams. Typical examples for t- and s-channel diagrams can be found in figure 2.4. In addition to an interaction through one boson directly connecting the incoming and outgoing vertices additional forms such as loop diagrams (see figure 2.3) or box diagrams are possible. Accordingly there are different diagrams with the same input and output. Only the properties of the incoming and outgoing particles can be measured. All other internal lines are called virtual particles. One diagram alone will not describe any process exactly. In fact the number of alternative diagrams is for any diagram infinite: it is always possible to add another internal loop. As a solution, approximations are used and the diagrams are organised in orders according to their significance for the process. Generally diagrams without any loops are called leading order diagrams and their cross-section is proportional to the related coupling constant squared. Any loop adds additional vertices and with them an additional factor depending on the squared

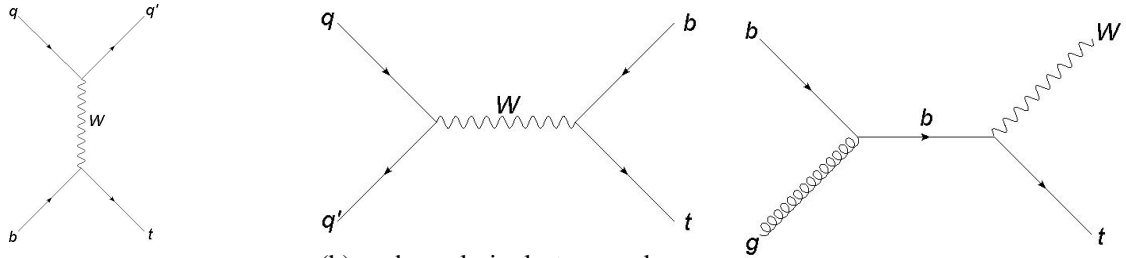

(a) t-channel single top production.

(b) s-channel single top production.

(c) Wt-production of a single top.

Figure 2.4: Single top-quark production at leading order

coupling constant. Accordingly the cross-section of the leading order is related to α^2, but one with one loop to α^4. Any diagram where the cross-section is proportional to α^4 is called next-to-leading order (NLO) diagram. Increasing the factor of the coupling constant further gives even higher orders. Since the coupling constant is very small for QED processes, the effect of the diagrams on the cross-section decreases rapidly with increasing orders. Accordingly, depending on the precision desired, very higher order diagrams can be neglected. For QCD processes this is more complicated due to the larger coupling constant. More information concerning this case can be found in Ref. [2].

Since these diagrams represent the different quantum field theories there are different rules which must be obeyed, depending on the interaction type in the Standard Model: all interactions must conserve electric and colour charge. The baryon number is also conserved: quarks are considered positive in this regard with a baryon number of $\frac{1}{3}$, antiquarks as negative ($-\frac{1}{3}$). Accordingly it is possible to gain one additional quark in an interaction if an additional antiquark is also created. The same is true for leptons: the lepton number is conserved. Finally flavour must be considered. This is a quantum number standing for the different types of quarks: up, down, strange, charm, bottom, top. So for example a strange quark has a flavour of S $= -1$, where the minus sign is due to historical reasons. This quantum number is conserved for strong and electromagnetic interactions, however not for weak interactions. There are different probabilities for different quarks to change into each other. These are formulated in the Cabibbo-Kobayashi-Maskawa (CKM) matrix [6]:

$$V_{CKM} = \begin{pmatrix} V_{ud} & V_{us} & V_{ub} \\ V_{cd} & V_{cs} & V_{cb} \\ V_{td} & V_{ts} & V_{tb} \end{pmatrix} \approx \begin{pmatrix} 0.97 & 0.23 & 0.00 \\ 0.23 & 0.97 & 0.04 \\ 0.01 & 0.04 & 1 \end{pmatrix} \tag{2.1}$$

So far changes of flavour have only been discovered in correlation with $W^{\pm}$ bosons. Much study is going into finding flavour changing interactions involving a Z boson, the so called flavour changing neutral currents (FCNC). They are often considered when searching for interactions, which the Standard Model does not predict – so called beyond Standard Model predictions, whose existence is not yet confirmed. More information on these and additional laws as well as the CKM matrix can be found in Ref. [3].

2.1.3 Useful variables

High energies are needed to create heavy elementary particles such as the top quark. In order to reach these, large set-ups must be used to create and observe them. One such facility is the Large Hadron Collider (LHC) with its different detectors. Both the LHC and the used detector will be introduced in Chapter 3. Beforehand it's important to consider what kind of information must be obtained to identify

the particles in question. One property is the mass of the particle, another its behaviour over time. One value to be considered here is the lifetime of a particle. Only very few particles do not decay into lighter particles and then only because conservation laws prevent it: the electron is the lightest charged particle and accordingly can not decay into anything lighter. The proton is stable as baryon number is conserved and it is the lightest baryon. Finally of course the photon is also stable as it does not have a mass. All other particles decay at some point if they are not bound as the neutron is in an atomic structure. Accordingly it is an important property of a particle how long it survives and how it decays. The lifetime τ depends on the kind of interaction involved in the decay. For strong interactions the lifetime is shortest at around $\tau_{\text{strong}} \approx 10^{-23}$ s while for weak interactions lifetimes of up to several minutes are possible. The lifetime is directly correlated to another very important property, the decay width Γ.

$$\Gamma = \frac{\hbar}{\tau} \tag{2.2}$$

The cross-section was already mentioned above. It is defined as:

$$\sigma = \frac{\text{number of interactions per unit time per target particle}}{\text{incident flux}} \tag{2.3}$$

The cross-section is related to the number of events, N, which can be measured:

$$N = \sigma \int \mathcal{L}(t)dt \tag{2.4}$$

The luminosity, $\mathcal{L}$, is defined as the number of particles passing per unit time and per unit area:

$$\mathcal{L} = \frac{nN_1N_2f}{A} \tag{2.5}$$

Here n is the number of bunches, N_1 and N_2 the number of particles per bunch and f the frequency of collisions. A bunch is a group of particles, which are kept together as a package and accelerated together. Finally A gives the cross-sectional area of overlap between the two bunches. The integrated luminosity, L, is defined as:

$$L = \int_0^t \mathcal{L}(t)dt \tag{2.6}$$

Comparing the measured cross-section with the theoretically predicted cross-section makes it possible to test theories.

2.2 Top quark physics

2.2.1 General aspects

With a mass of $m_t = 173.21 \pm 0.51(\text{stat}) \pm 0.71(\text{sys})$ GeV [6]. the top quark is the heaviest quark in the Standard Model and is almost as heavy as a gold atom. Due to this the top quark was only discovered in 1995 at the Fermilab Tevatron, even though it was postulated by Kobayashi and Maskawa in 1973 [3],. Because of its very short lifetime of only 5×10^{-25} s the top quark decays before it can form bound states. This unusual property gives it an important role in modern research. Since its decay products can be observed directly in particle detectors, instead of only the decay products of the formed hadron, it is possible to measure the top-quark properties such as its mass at high precisions. In addition its quasi-free behaviour allows for the spin information to be carried on to its decay products [8]. Finally the top quark

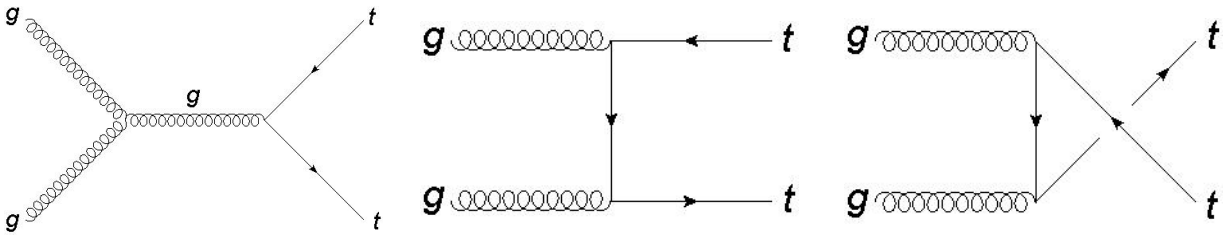

Figure 2.5: Top-quark pair production due to gluon fusion at leading order.

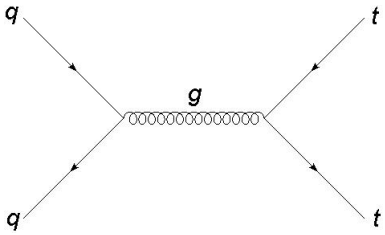

Figure 2.6: Top-quark pair production due to quark-antiquark annihilation at the leading order.

makes it possible to study beyond Standard Model predictions such as flavour changing neutral currents. Its electric charge is, as already mentioned in table 2.1, Q = +2/3e.

2.2.2 Top production and decay

There are two different possibilities for top-quark production: a top-quark pair or a single top-quark can be produced. The possible processes for a top-quark pair production are gluon fusion (see figure 2.5) and quark–antiquark annihilation (see figure 2.6). At the LHC at $\sqrt{s}$ =13 TeV gluon fusion dominates with a probability of 90 %. The cross-section for top-quark pair production at the LHC at $\sqrt{s}$ =13 TeV at NNLO with an assumed top mass of 173.2 GeV c^{-2} is $\sigma_{t\bar{t}}$ = (816 $^{+19}_{-29}$ (stat.) ± 34 (sys.)) pb. The single top-quark production is less likely, but also possible. Here there are three different production modes possible, all involving a Wtb vertex. Out of the three – the s-channel, the t-channel and the Wt-production (see figure 2.4) – the t-channel is the most probable. Its cross-section at $\sqrt{s}$ = 13TeV for an assumed top mass of 172.5 GeV was measured to be σ_{tq} = (156 ± 5 (stat.) ± 27 (sys.) ± 3 (lumi.)) pb for single top-quark production and $\sigma_{\bar{t}q}$ = (91 ± 4 (stat.) ± 18 (sys.) ± 2 (lumi.)) pb for single top-antiquark production [9].

In addition there are rare productions. Two of them are the production of the top quark in association with a Z boson ($pp \rightarrow tZq$), which will be studied in this thesis, and the production of the top quark in association with a Higgs boson ($pp \rightarrow tHq$). Their Feynman graphs can be found in figure 2.7 and figure 2.8. The LHC makes studying these rare productions possible due to its high energy and integrated luminosity [1]. The tZq production allows probing of both the WWZ couplings and the tWb couplings. It is also a background for the tHq production. First evidence for this rare production was found in 2017 with a signal significance of 4.2 σ. The measured cross-section is σ_{tZq} = (600 ± 170 (stat.) ± 140 (sys.)) fb [1]. This analysis is performed on a different final state, the so called trilepton channel.

2.2.3 tZq final states

As mentioned above, the top quark is not a stable particle. The CKM matrix elements corresponding to the top quark have been measured. While V_{td} and V_{ts} are close to zero, V_{tb} is almost 1. Due to this, the top quark decays almost exclusively to a bottom quark and a W boson. However the W boson is

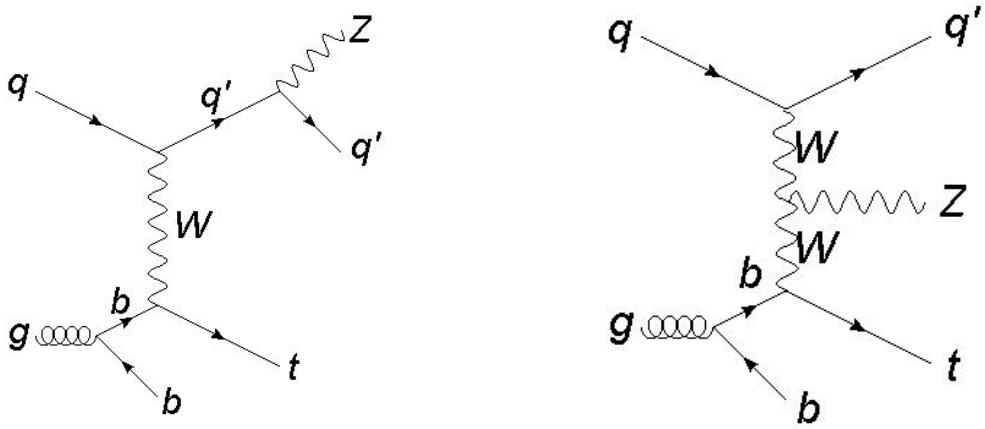

Figure 2.7: Single top production in association with a Z boson.

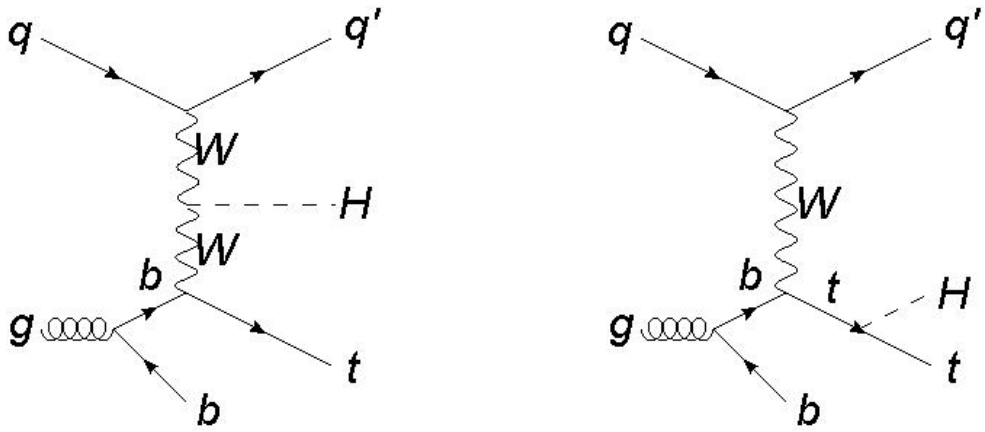

Figure 2.8: Single top production in association with a H boson.

an unstable particles and will decay further. It decays either into two quarks with a branching ratio of (67.41 ± 0.27) %[6] or into two leptons. In the case of the dileptonic tZq channel the W boson must decay hadronically to gain the desired final state. The Z boson too is unstable and can decay into two leptons or two quarks. Besides the trilepton channel mentioned above there are additional channels, which are each named after the number of leptons in the final state. In the case of the dilepton channel, which is studied in this thesis, two leptons are observed. In order to observe them the Z boson must decay leptonically. The branching ratio of the Z boson decaying into a charged lepton pair is (10.10 ± 0.02) % [6]. The end products of the tZq dilepton channel are two leptons coming from the Z boson and four quarks out of which one is a b quark (see figure 2.9). To check how well theory predictions match the measured data, the signal strength is often used. It is a factor with which the Standard Model prediction must be multiplied in order for the predicted values and the observed data to match within a certain confidence level (see Chapter 6). If the Standard Model prediction is accurate it is 1.

2.2.4 Backgrounds

There is the possibility of other interactions producing a similar final state as that of the tZq dilepton channel. Because of this they are hard to separate from the signal events and accordingly contribute to the background events. Several different background sources have been identified. Any process containing

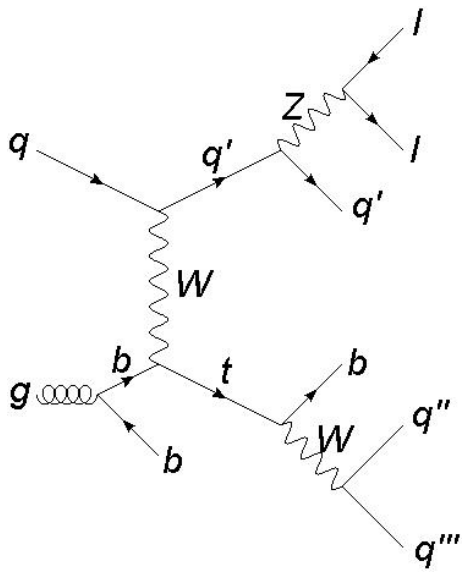

Figure 2.9: Dilepton channel of the single top production in association with a Z boson.

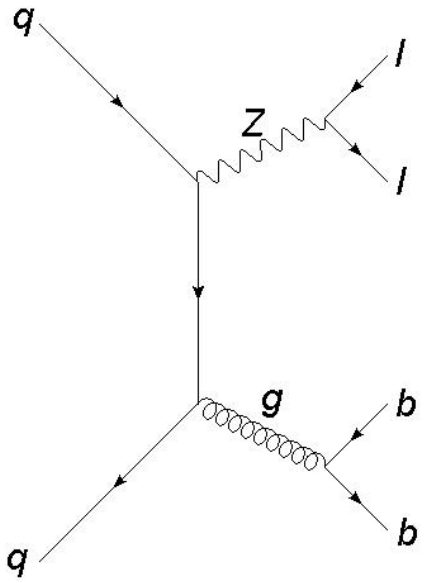

Figure 2.10: Possible Feynman diagram of Z+Jets background.

Z or W bosons decaying into the necessary two leptons can be responsible for the production of a final state similar to the signal one. Due to the possible Z- and W-boson decays a background must contain at least one Z boson or two W bosons to create two leptons. Some of the quarks can be obtained from radiation of gluons or the decays of heavier quarks to lighter ones by radiating a boson, which then decays into further quarks. The number of possible backgrounds is further extended by the fact that neutrinos can not be detected directly and that the identification of the b quark by the experiment is not perfect. Accordingly it is possible for a different quark to be misidentified as a b quark.

One possible background is the production of a Z boson in association with several quarks or gluons, where the Z boson decays leptonically (see figure 2.10 for an example). Such backgrounds are called "Z+jets" backgrounds. Alternatively it is possible to have not just one boson, but several bosons instead. Either a single Z boson in combination with a hadronically decaying W boson or two leptonically decaying W bosons are possible. In addition two Z bosons with one decaying hadronically and the other leptonically are also possible. These processes are called diboson backgrounds. Another possible source could be $t\bar{t}$ production, when both top quarks decay into two W bosons and two b quarks. There are several further backgrounds, which can cause simliar signatures such as $t\bar{t}+W$, $t\bar{t}+Z$, $t\bar{t}+H$, Wt or tWZ.

CHAPTER 3

LHC and the ATLAS detector

In this chapter the experimental set-up is introduced shortly. The information for section 3.1 is summarised from Ref. [10]. Details concerning the detector can be found in Ref. [11] unless stated otherwise.

3.1 CERN and the LHC

The European Organisation for Nuclear Research CERN (Conseil Européen pour la Recherche Nucléaire) has its main international research centre close to Geneva on the border between Switzerland and France. The Large Hadron Collider (LHC) is the most recent addition to the accelerator complex and the world's most powerful accelerator. Located between 50 m and 175 m below the ground, the 27 km long structure will accelerate protons so that their collisions reach centre of mass energies of up to $\sqrt{s} = 14\,\text{TeV}$. It is upgraded in several steps until the set-up reaches its final design operation conditions. Currently collisions of two protons with centre of mass energies of 13 TeV have been recorded. Alternatively lead ion collisions can also be caused with centre of mass energies of up to 1 150 TeV.

In the case of proton acceleration hydrogen is used as the particle source. After their production the protons are accelerated at the Linear Accelerator 2 (LINAC2) before entering the Proton Synchrotron Booster (PS Booster) with an energy per proton of 50 MeV. Passing two additional circular accelerators, the Proton Synchrotron (PS) and the Super Proton Synchrotron (SPS), the particles are accelerated to an energy of 450 GeV. As a final step the particles are accelerated in approximately 20 min to energies of 7 TeV at the LHC (see figure 3.1). At the LHC groups of $\sim 10^{11}$ particles, so called bunches, are accelerated together. One proton beam consist of 2808 such bunches. In order to reach the intended energy superconducting magnets and cavities are needed to guide and collimate the beam. In total roughly 9600 magnets are used, which are cooled down with liquid helium to $-271.3\,^{\circ}\text{C}$. At the LHC the desired peak luminosity is $1.2 \times 10^{34}\,\text{cm}^{-2}\text{s}^{-1}$. At each one of the four collision points one of the four main detectors are placed. The detectors are: ALICE, ATLAS, CMS and LHCb.

The ALICE experiment uses lead ion collisions to study the properties of quark-gluon plasma in order to gain a better understanding of the creation of the universe. Both the ATLAS and the CMS detectors are multi-purpose detectors which mainly focus on proton collisions. Finally the LHCb detector concentrates on physics involving b quarks. The asymmetry between matter and antimatter in B-particles is considered here to study why the universe is made up of the matter observed. There are three additional, smaller experiments positioned close to the four main experiments: LHCf, MOEDAL and TOTEM.

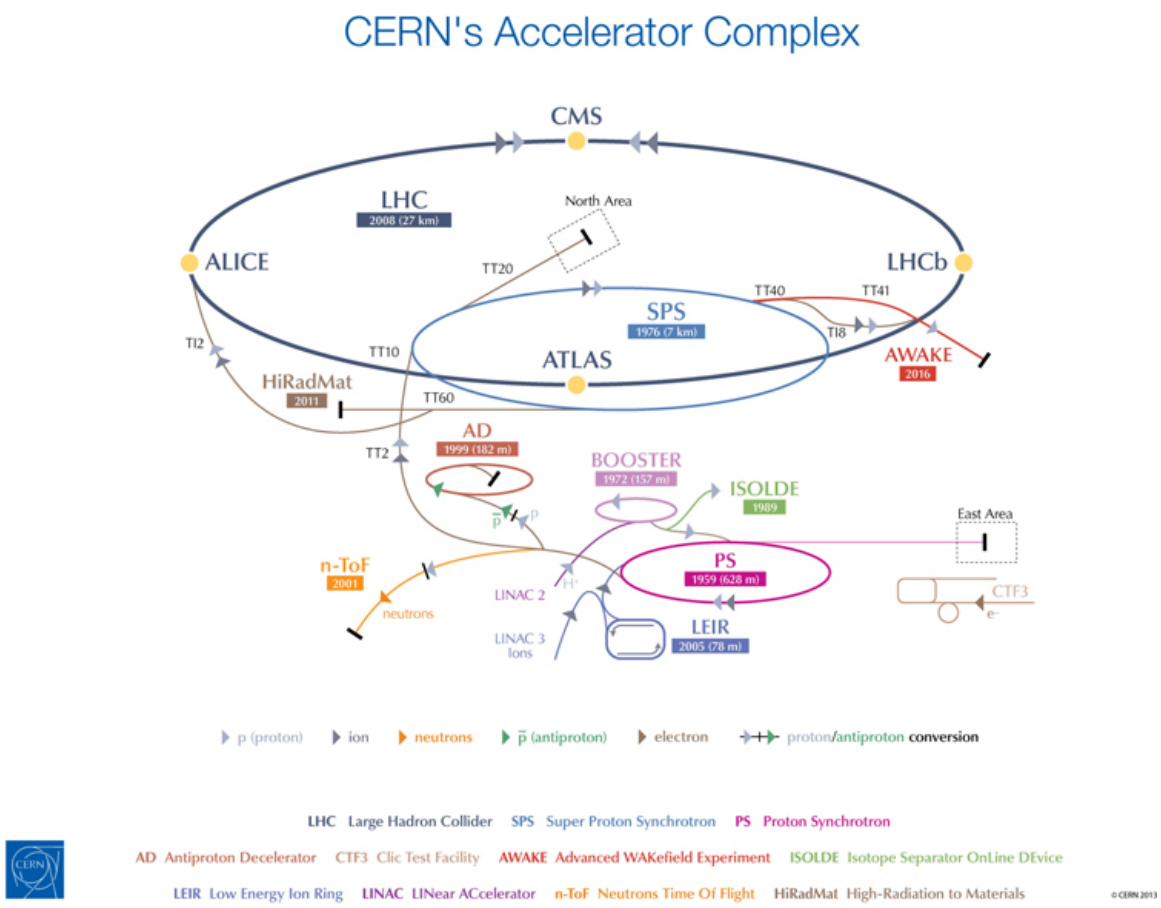

Figure 3.1: The CERN accelerator complex with the accelerator chain of the LHC [12].

3.2 Particle identification in detectors

Large detectors such as ATLAS or CMS are employed to gain information about the collisions created by the LHC. Said information must be collected from different detector parts and combined to give a full view of the collision. There are several different parameters of interest, such as the so called vertex point: often a collision causes not only one particle interaction, but several. When a high number of simultaneous vertices is created it is called pile-up. In order to make it possible to differentiate between the different interactions, the position where it took place, the primary vertex point, must be established. Accordingly it is necessary to know the path ("track") along which the different particles travel. In typical particle detectors the innermost detector is a tracking detector, which allows for a precise determination of the path of charged particles. By measuring several points where the particle passed, its track can be reconstructed. A magnetic field is employed in the inner detector which bends the tracks of the charged particles, making it possible to gain information about their charge and momentum. In addition to the path, information about the energy of the different particles is needed. For this so called calorimeters are important as most particles deposit their energy here, making it possible to measure it. Only muons and neutrinos do not deposit all or most of their energy in the calorimeters. While neutrinos do not interact with the calorimeters at all, muons do deposit some of their energy in the calorimeter, but not all of it. In the case of muons, a muon spectrometer with a magnetic field in addition to the information from the tracker makes energy measurements possible. Finally the particle type must be identified. Figure 3.2

gives an example for particle identification for commonly known particles at the ATLAS detector, which is a typical particle detector. Depending on where a particle is stopped a first differentiation can be made between hadrons and photons, electrons and muons. The next differentiation can be made depending on whether a particle has a charge or not: neutral particles such as neutrons, photons and neutrinos leave no tracks. Accordingly it is possible to differentiate between photons and electrons as well as protons and neutrons. The sign of the charge is taken from the curvature of the track. The only known particles passing through all detectors are muons and neutrinos. They can be differentiated since muons leave tracks in the inner detectors and deposit some of their energy in the calorimeters, while neutrinos do not. Muons are also the only particles leaving hits in the muon detector. Neutrinos can not be measured directly. Instead their energy can be reconstructed using momentum conversation in the transverse plane.

It should be noted that even though the mentioned particles are commonly known, they are only a small representation of the particles observed at ATLAS. Neither the identification of bosons nor of additional hadrons is described. Some of them are too unstable and decay before reaching the calorimeters, while others have long enough lifetimes to cause showers directly. As an example charged and neutral pions are introduced, since they are some of the most commonly produced particles: while charged pions have a large enough lifetime to reach the calorimeter and create hadronic showers, neutral pions do not. They decay with a probability of 99.99 % into two photons, which will then cause electromagnetic showers. Said photons can be identified as coming from the same vertex and their invariant mass will be used to reconstruct the neutral pion.

3.3 ATLAS detector

The ATLAS (A Toroidal LHC Apparatus) detector is positioned at the Meyrin site in Switzerland, roughly 100 m underground. It has a cylindrical shape (46 m long, 25 m in diameter) and is the largest volume detector in the world (see figure 3.3). With a weight of 7000 tonnes the detector weighs roughly as much as the Eifel Tower. It is centred around one of the interaction points of the LHC collider and structured like an onion with different sub-detectors positioned around the collision point. The coordinate system used for describing the positions at ATLAS is shown in figure 3.4. The sub-detectors are the inner detector, the calorimeters and the muon spectrometer. In addition, a magnet system is employed to create magnetic fields. There are in total four magnet systems installed in the ATLAS detector. Three of them are toroids and one a solenoid system. The solenoid system provides the magnetic field of 2 T for the inner detector. The three toroids provide a magnetic field with an integral between 2.0 and 6.0 T m across most of the detector. The detector can be split into the barrel, positioned at low $|z|$ and the end-caps, which are placed further from the interaction point. Since over a billion particle interactions are observed in a single second, it is necessary to filter out only the most interesting events for saving. Filtering and saving is done by the trigger and data acquisition system. The different detectors will be introduced in detail in the following sections.

3.3.1 Inner detector

The inner detector has a length of roughly 7 m. It has a diameter of 2.3 m and consists of three sub-detectors, which are placed around the collision points (see 3.5). The Silicon Pixel Detector is positioned closest to the interaction and in the barrel region followed by a Semiconductor Tracker (SCT) and finally a Transition Radiation Tracker (TRT). As shown in figure 3.5 each of these detectors also have an end-cap at larger $|z|$. The inner detector is optimised for hermetic and robust pattern recognition, primary and secondary vertex measurements as well as high momentum resolution above the p_{T} threshold of 0.5 GeV

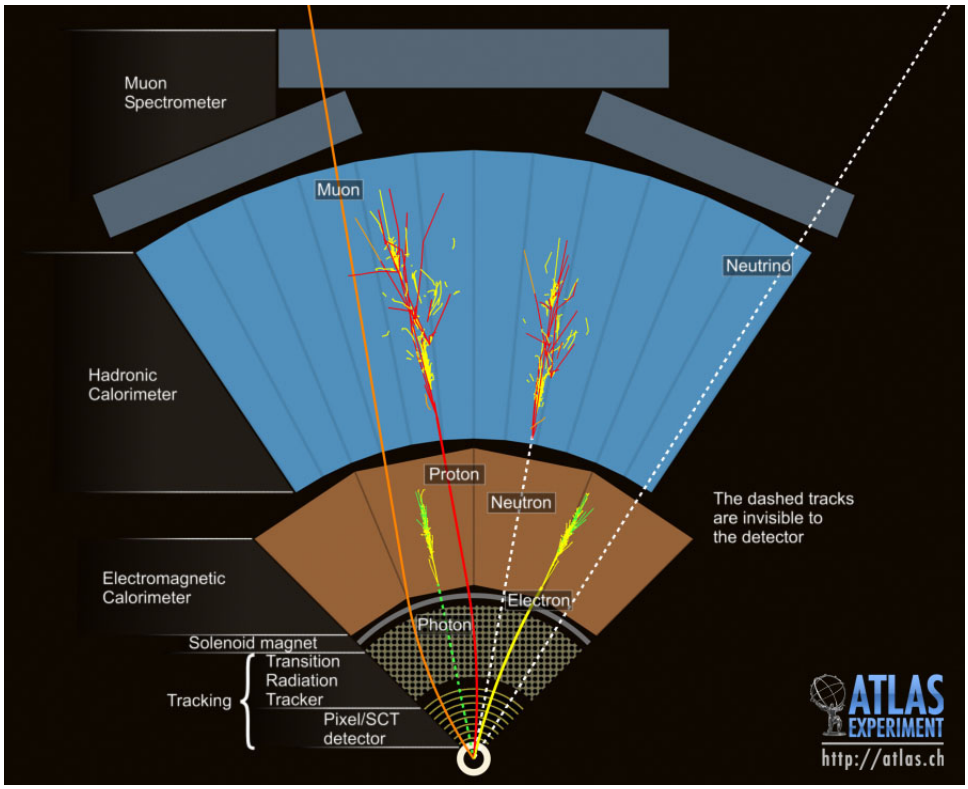

Figure 3.2: Particle identification at the ATLAS experiment [13].

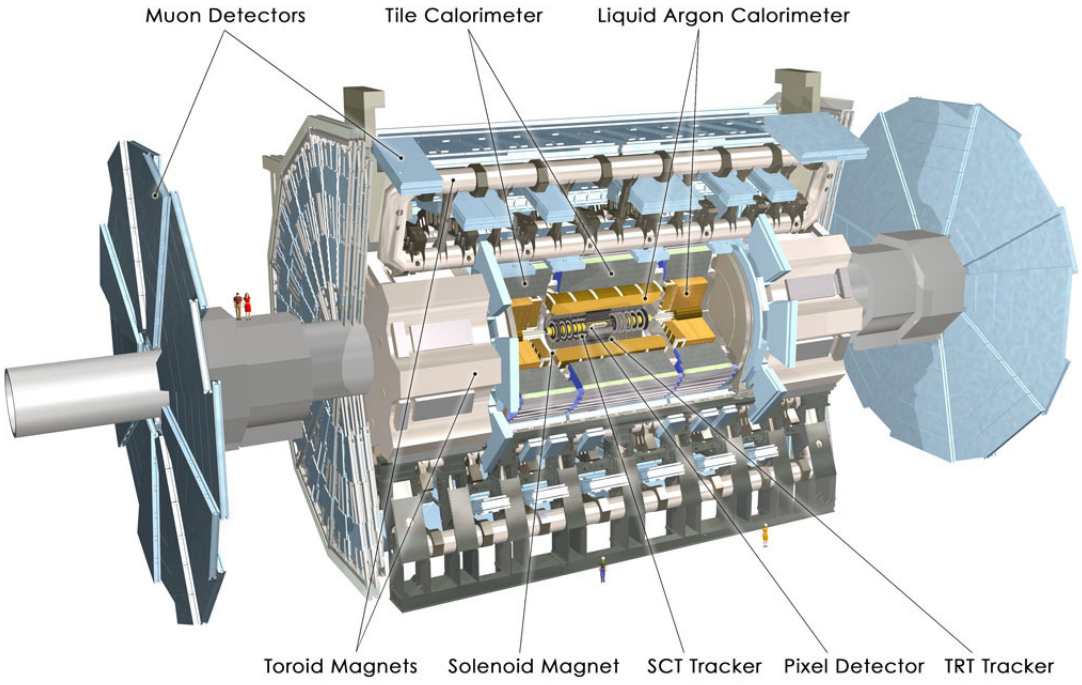

Figure 3.3: The ATLAS detector [11].

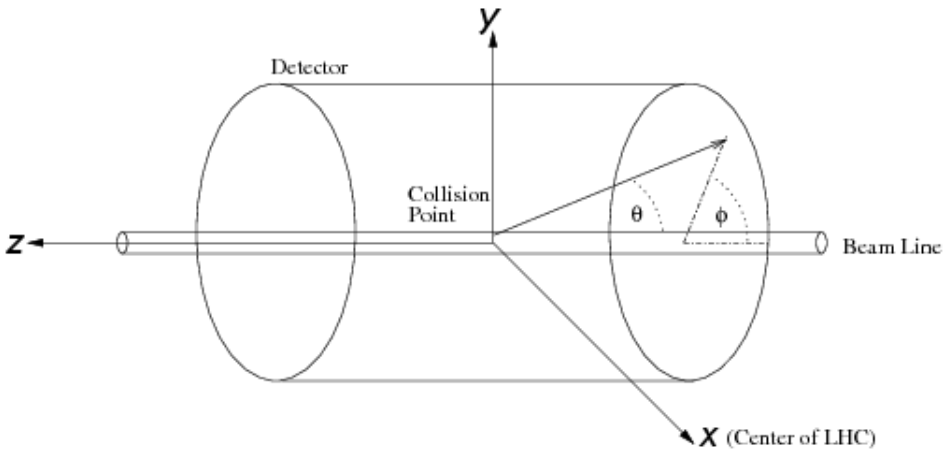

Figure 3.4: Coordinate system used at the ATLAS experiment [14].

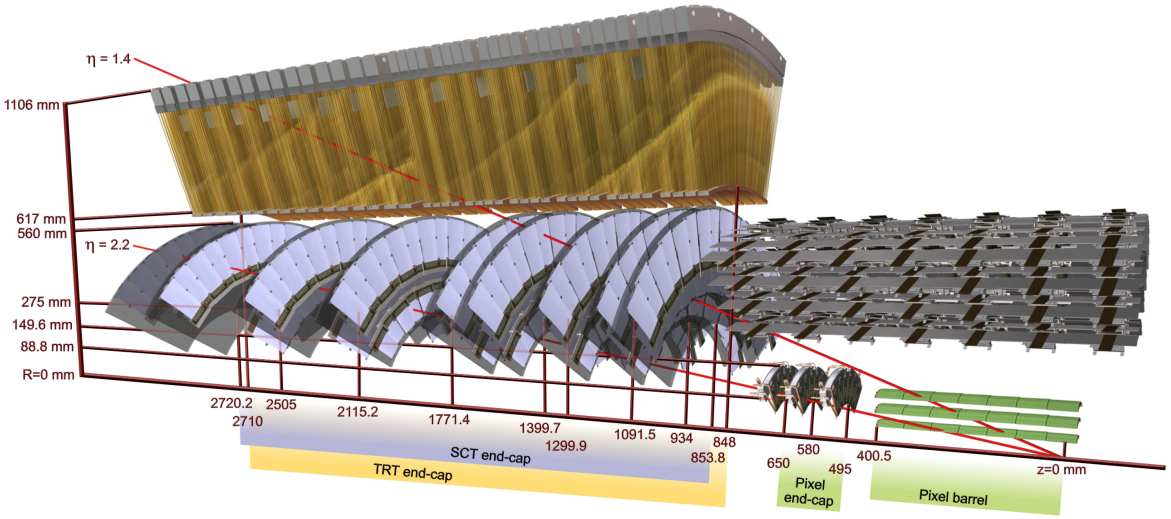

Figure 3.5: Image showing the setup of the different layers of the inner detector of the ATLAS detector before inclusion of the IBL detector [11].

and at a pseudorapidity of $|\eta| < 2.5$[1]. At larger $|\eta|$ due to the positioning of the beam pipe the precision decreases.

Both the Pixel and the SCT detector are silicon-based detectors. If a passing particle deposits energy in the silicon structure, electrons are freed from their lattice and due to a voltage being applied an electric current can be measured. The detectors provide good enough energy and time resolutions that out-of-time pileup is not an issue [15]. In the case of the Pixel Detector oxygenated n-type wafers are used with readout pixels placed on the n^+-implanted side of the detector. It consists of four layers. For the outer three layers 90 % of the pixels measure $50 \cdot 400 \mu m^2$. In the R-ϕ plane the position resolution is 10 μm and along the z-axis (R) 115 μm [16]. The innermost layer is called the Insertable B-Layer (IBL) detector [17]. It is a newer addition to the Silicon Pixel Detector, which was installed after Run~1[2] and not included in figure 3.5. It is positioned at ~ 3.3 cm from the beam line and consists of 14 structures which are each loaded with 20 hybrid pixel detector modules. The SCT consists of 15912 sensors which, different from the pixel detector, use a classic p-n technology. Each sensor contains 770 active readout strips. The R-ϕ spacial resolution is 17 μm and in z/R direction 580 μm [16]. Together the two detectors provide at least eight hits at a pseudorapidity of $|\eta| < 2.5$.

The outermost detector of the inner detector is the Transition Radiation Tracker, which adds at least 30 additional hits per charged particle with a pseudorapidity of $|\eta| < 2.1$. It consists of straw tubes filled with a gas mixture of Xe, CO_2 and O_2. A wire is positioned in the middle of each tube serving as anode, while the straw walls serve as cathode. The change of potential caused by charged particles causing ionisation as they travel within the tube can then be measured. In order to identify electrons a radiator is placed between the straws. Transition radiation is emitted, when electrons pass between the radiator and other materials. Said radiation can be detected using the xenon gas. The transition radiation deposits more energy than if a charged particle is merely passing through the tube, making a separation possible. Each straw has a diameter of 4 mm. The roughly 50000 tubes of the barrel are positioned parallel to the beam pipe. For the end-caps, 320000 tubes are placed in radial direction. Accordingly along the barrels the z-position can not be measured by the TRT detector and in the endcaps the radius can not be measured [18]. In the R-ϕ plane the intrinsic accuracy is 130 μm per straw [16].

3.3.2 Calorimeter system

The ATLAS detector contains two different types of calorimeters: the electromagnetic calorimeter (ECAL) and the hadron calorimeter (see figure 3.6). The calorimeters are constructed in such a way that hadrons, electrons, positrons and photons deposit their energy in the structure. When particles pass through matter they can interact with said matter and cause the production of additional, less energetic particles. These too can interact and create even further particles until the particles do not contain enough energy anymore to continue the process. This group of particles is called a particle shower. The shower is stopped and its particles absorbed, making energy measurements possible. The two different detectors are optimised such that they either mainly stop electromagnetically interacting particles such as electrons and photons or mainly strongly interacting hadrons. By measuring the energy and the area in which the particle deposited its energy it is possible to differentiate between hadrons and other particles. In addition, due to the wide range of pseudorapidity ($|\eta| < 4.9$) covered and the good precision of the energy measurement, it is possible to calculate the missing transverse energy (E_T^{miss}). In order to ascertain that all showers are stopped in the calorimeter the calorimeters are roughly 10 interaction lengths thick. The

[1] $\eta = -\ln(\tan(\theta/2))$

[2] Run~1 took place from March 2010 until early 2013. After two years of upgrading the accelerator and detectors Run~2 began in early 2015 at $\sqrt{s} = 13$ TeV

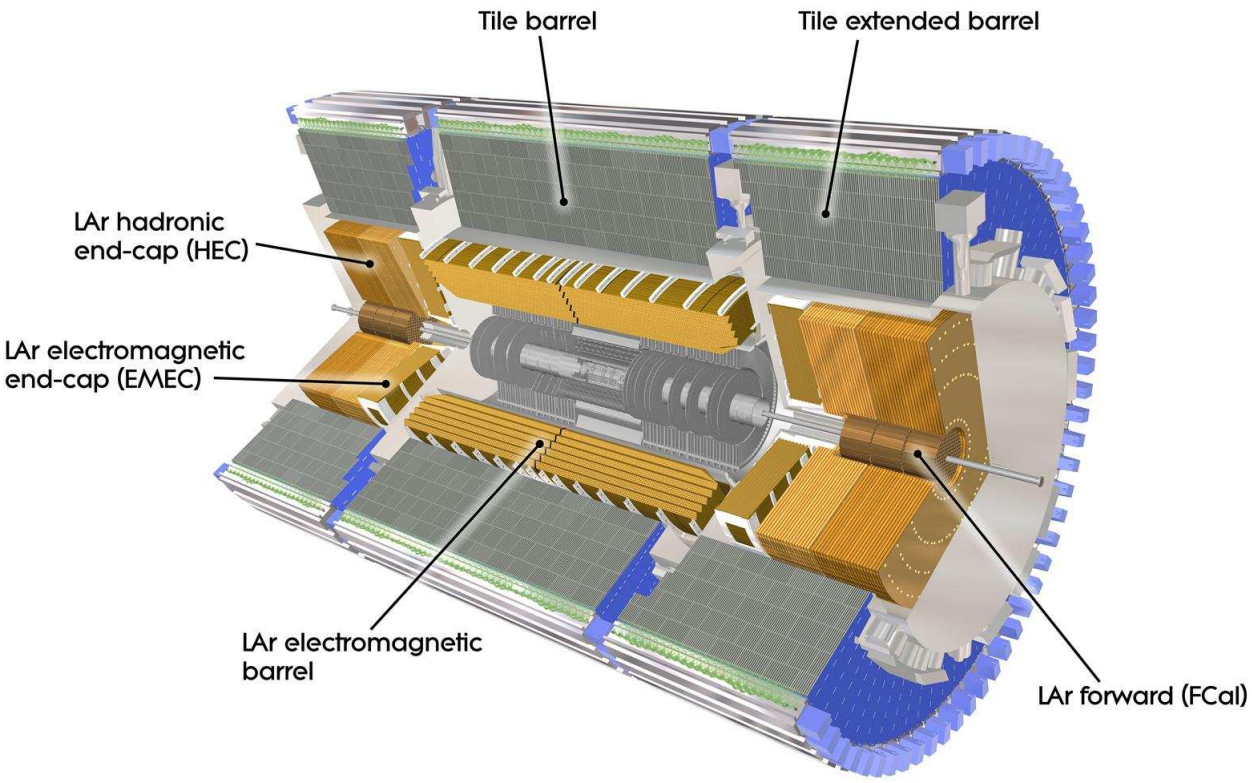

Figure 3.6: The calorimeter of the ATLAS detector [11].

interaction length is the mean path required to reduce the number of charged relativistic particles by a factor of 1/e.

The electromagnetic calorimeter contains a barrel part as well as two end-caps. It uses lead as an active material and liquid argon (LAr) to create the showers. The barrel is divided into two identical half barrels and covers the pseudorapidity of $|\eta| < 1.475$. The two barrels are placed to the right and left of $z = 0$, causing a small gap of 4 mm at $z = 0$. The end-caps are divided into two wheels, the outer covering a range of $1.375 < |\eta| < 2.5$ and the inner covering a range of $2.5 < |\eta| < 3.2$.

The hadron calorimeter can be split into three different parts: the Tile Calorimeter, the LAr Hadron End-Cap Calorimeter and the LAr Forward Calorimeter. The Tile Calorimeter uses scintillating tiles as active material and steel to create the showers. It covers the barrel region of $|\eta| < 1.0$ and the extended barrel region of $0.8 < |\eta| < 1.7$. The LAr Hadron End-Caps are split into two wheels, placed after each other in z direction. It overlaps in the pseudorapidity range with the tile as well as the forward calorimeter covering a range of $1.5 < |\eta| < 3.2$. Finally the LAr Forward Calorimeter covers the area of $|\eta| > 3.1$ to $|\eta| = 4.9$. Due to a reduced length of the forward calorimeter a high density design is necessary. It consists of three parts: the first one uses copper for electromagnetic measurements and the other two tungsten for hadronic measurements. Liquid argon serves as the active material.

The uncertainty of the energy measured in the two detectors depends on the particle type as well as the $|\eta|$.

3.3.3 Muon spectrometer

The following information is summarised from Ref. [19]. As already mentioned above muons and neutrinos are the only particles which are not be stopped by the calorimeters, due to their low interaction cross-section with material. In order to measure the momenta of the muons and to assure their correct identification, the muon spectrometer is used. The muon spectrometer consists of four different detector types: Monitored Drift Tubes (MDT) and Cathode Strip Chambers (CSC) are used for the momentum measurements, while Resistive Plate Chambers (RPC) and Thin Gap Chambers (TGC) are employed for triggering. The momenta are calculated using the track curvatures.

The Monitored Drift Tubes are aluminium tubes filled with a mixture of Ar CO_2. They have a diameter of 30 mm with a wire spun in the middle. They follow the same basic concepts as the straw tubes of the TRT detector. The modules are arranged in three coaxial layers in the barrel region and as four discs for the end-caps. A muon hitting the spectrometer in the MDT area hits about 20 tubes before exiting the spectrometer. The MDT cover the pseudorapidity range $|\eta| < 1$ for the barrel and $1 < |\eta| < 2.0$ for the end-caps. The CSC system takes over for the range of $2.0 < |\eta| < 2.7$. Different from the MDTs the CSCs are multi-wire proportional chambers. Here one chamber contains several wires. While the wires serve as anodes the chamber walls serve as cathodes. The gas used is a mixture of Ar, CO_2 and CF_4.

Triggering is done by the RCPs for the barrel region ($|\eta| < 1.05$) and by the TGCs for the end-caps ($1.05 < |\eta| < 2.7$). The RCPs consists of two parallel plates with a gas in between them. The gas is a mixture of mainly $C_2H_2F_4$ and a small portion of SF_6. The modules have a space-time resolution of $1\,\text{cm} \cdot 1\,\text{ns}$ with digital readout. Finally the TGCs are similar to the CSC system, except that the spacing between two anode wires is larger than between anode and cathode. For multi-wire proportional chambers the opposite would be the case. A mixture of CO_2 and n-C_5H is used.

3.3.4 Trigger and data acquisition system

The following information on the Run~2 trigger system is summarised from Ref. [20]. At the current design luminosity a bunch crossing rate of 40 MHz is expected. However, current technology does not allow for saving events at such a high rate. In addition many of the observed events are not of interest. Accordingly only a smaller subset is saved for detailed analysis. Two trigger systems choose which events are to be saved: the hardware-based Level 1 trigger and the software-based High Level Trigger (HLT). The Level 1 trigger is limited to an output rate of 100 kHz and is given 2.5 μs to make its selection and distribute the decision. In order to make such a fast selection possible the trigger only considers information at reduced granularity from the calorimeters and the muon spectrometer. The events selected by the Level 1 trigger are buffered in the Read-Out System (ROS). In addition the Level 1 trigger chooses "Regions of Interest" (RoIs) and passes their information to the High Level Trigger. The High Level Trigger uses complex algorithms to further reduce the event rate from 100 kHz to approximately 1 kHz on average. It has a processing time of about 200 ms. Both the RoIs as well as the full event are available to the HLT at full granularity. After passing the HLT the events are transferred to local storage.

The described trigger system is an update of the original trigger system employed during Run~1. It was installed during the first long shut-down between Run~1 and Run~2. Due to this parts of the updated trigger were not fully operational yet in 2015 [21] leading to some selection differences between 2015 and 2016 (see chapter 4.2).

CHAPTER 4

Object reconstruction and data sets

4.1 Object reconstruction

The process of particle identification was roughly explained in chapter 3.2. This chapter focuses on taking a detailed look at object reconstruction. The exact object definitions used for this analysis are discussed below.

Due to the high luminosity of the LHC it is likely that not only one vertex is registered. One vertex candidate is chosen as the one be to be focused on - the so called primary vertex. It is the vertex candidate with the highest sum of squared transverse momenta[1]. The sum contains all associated tracks with at least 400 MeV.

Electrons

Electron reconstruction is done in the central region of $|\eta| < 2.47$. However in the area of $1.37 < |\eta| < 1.52$, where the electromagnetic calorimeter barrel and the end caps meet, a lot of material is positioned in front of the first active calorimeter layer. Accordingly this area is excluded. The chosen $|\eta|$ range of the electromagnetic calorimeter is searched for calorimeter cells with transverse energies[2] above 2.5 GeV, so called seeds. In addition a pattern recognition program looks for tracks with at least 7 hits in the silicon detectors. An algorithm attempts to match the measured tracks with the seeds. The tracks are extrapolated to the middle layer of the electromagnetic calorimeter. If an extrapolated track is found within $\Delta\eta < 0.05$ and $\Delta\phi < 0.1$ of a seed [22] it is matched to the seed. Electron candidates without any matching track are removed as electron candidates and are instead considered as photon candidates. Electron candidates must also fulfill a requirement on the total transverse energy of $E_{\mathrm{T}} > 15$ GeV. In order to reduce the amount of non-electron objects being identified as electrons an identification algorithm is applied. The algorithm uses information such as measurements from the Transition Radiation Tracker, the calorimeter shower shapes and track properties. Bremsstrahlung effects and hits in the innermost pixel layer are also employed. This algorithm is applied so that in the case of a $Z \rightarrow e^+e^-$ event it has an efficiency of identifying electrons of 80 %. 700 jets are rejected for one accepted jet at $p_{\mathrm{T}} = 40$ GeV. In addition an isolation requirement is also set to discriminate further between signal and background. An isolation efficiency of 90(99) % for $p_{\mathrm{T}} = 25(60)$ GeV is chosen [23].

[1] $p_{\mathrm{T}} = \sqrt{p_x^2 + p_y^2}$

[2] $E_{\mathrm{T}} = \sqrt{p_{\mathrm{T}}^2 + m^2}$

Muons

Similar to the electron reconstruction only objects with $|\eta| < 2.5$ and with a total transverse energy of $E_T > 15$ GeV are considered. Tracks are reconstructed in the inner detector and in the muon spectrometer independently. Afterwards the track in the muon spectrometer is fitted to the matching track of the inner detector. At least two stations of the muon spectrometer must register a signal. In addition the normalised χ^2 of the combined track fit must be less than 8. The reconstruction efficiency was measured for W bosons decaying to muons for $20 < p_T < 100$ GeV. It is 96.1 %. The rejection of non-prompt muons coming from hadrons decaying in flight is 600 rejected muons for each accepted one. An additional isolation criteria is applied to decrease the amount of wrongly identified particles. It uses the fact that many muons originating from the decay of heavy particles are produced isolated. The applied gradient working point gives an efficiency of 90(99) % at 25(60) GeV [24].

Jets

For the reconstruction of jets, the anti-k_t algorithm is used (see Ref. [25] and Ref. [26]). It is an algorithm which calculates the distances between all jet candidates depending on the distance in η, ϕ and the value of the momenta. The pair of jet candidates with the smallest distance are combined, if a radius parameter is fulfilled. Alternatively the jet candidate can be identified as a "final jet" coming from the interaction point. If it is not a "final jet" the combined candidate is returned to the list and the process repeated. In ATLAS the radius parameter is R=0.4. Only jets with a $p_T > 30$ GeV and within $|\eta| < 4.5$ are considered. Imperfections of the detector lead to position and p_T dependent measurements, which have to be corrected. This is done using Monte Carlo based simulations and *insitu* techniques (see Ref. [27]). Finally considerations must be made for the case that a jet does not actually originate from the hard scattering vertex of the event. For this the Jet Vertex Tagger (JVT) is applied [28]. It is a discriminant, which is constructed with a two dimensional likelihood method. The JVT is chosen so that for jets with $E_T < 60$ GeV and $|\eta| < 2.4$ an efficiency of 92 % is reached for jets coming from the hard scattering vertex. At the same time 98 % of the jets coming from pile-up or noise are rejected.

Additional consideration must be made for jets containing a b hadron, as a b-quark being part of the final-state particles is an important differentiation factor. The so called "b-tagging" is a method which associates a discriminator with each jet. A higher efficiency at recognising a b hadron at the same time means a higher misidentification. A multivariate analysis is used to make the differentiation [29]. It uses properties such as the b hadrons' long lifetimes and high masses [29]. The inner detector is used in the process, because of which b-tagging is only possible at $|\eta| < 2.5$. In addition the transverse momentum must be larger than 20 GeV. Possible b-tagging efficiencies are for example 77 % and 70 %. The mistag rate for a b-tagging efficiency of 70 % is for $p_T^{\text{Jet}} < 200$ GeV roughly 1 % [29].

4.2 Data samples

For the data sample the combined samples of 2015 and 2016 data-taking are used. The centre-of-mass energy during these two years of data taking is $\sqrt{s} = 13$ TeV. Together the two data-taking periods have an integrated luminosity of 36.1 fb^{-1}. Either the electron or the muon trigger must accept the event.

In 2015 [30] electrons had to have a transverse energy of at least 24 GeV to be accepted by the trigger. Single muons had to be isolated and have an $E_T > 20$ GeV. Alternatively they could be non-isolated if they had a transverse energy of at least 50 GeV. In 2016 [31] the electrons had to be isolated and satisfy a "tight" identification. In addition they had to have an $E_T > 26$ GeV. Alternatively "medium" electrons with an $E_T > 60$ GeV were also accepted. Muons had to either be isolated and have an $E_T > 26$ GeV or have an $E_T > 50$ GeV (see 4.1).

	Electrons		Muons	
year	E_T	condition	E_T	condition
2015	24 GeV		20 GeV	isolated
			50 GeV	non-isolated
2016	26 GeV	isolated, "tight"	26 GeV	isolated
	60 GeV	"medium"	50 GeV	non-isolated

Table 4.1: Conditions for data sets used for the analysis dependent on the year they were taken.

4.3 Monte Carlo samples

Monte Carlo simulations are required to test the predictions made by the Standard Model against measurements. In order to produce them, several different event generators are employed both at leading and at next-to-leading order. Due to the complex structure of the protons containing not only the three valence quarks, but also sea quarks, so called Parton Distribution Functions (PDFs) describing the momentum of the considered parton are required as input for event generators. Since the type of hard-scattering process is dependent on the energy of the partons involved, the PDFs are an important input for the scattering process. With the PDFs the hard-scattering process is simulated for a top mass of $m_{top} = 172.5\,\text{GeV}$. Once the hard-scattering process has been simulated the further decay of the produced particles is also simulated. Hadronisation processes are also simulated. In order to take into account the particle interaction with the detector and the imperfections of the ATLAS detector the simulated events are passed through a Geant4-based detector simulation [32]. This results in simulated events with properties which closely mirror the actual data. All of the Monte Carlo samples are normalised to their respective standard model cross-sections. In most cases the normalisation was done at NLO. More details can be found in the appendix in tables B.2 and B.3.

The tZq sample was simulated at leading order. For the PDFs CTEQ6L1 [33] was used and as generator MadGraph 5.2.2 [34]. Pythia 6 [35] served for simulating the hadron shower and the hadronisation using the Perugia 2012 [36] set of tuned parameters. The event kinematics of the used LO simulation agrees with the NLO simulation within 10 % before parton showering. Accordingly it is possible to rescale the leading order cross-section $\sigma_{tZq} = (600 \pm 170\,(\text{stat.}) \pm 140\,(\text{sys.}))\,\text{fb}$ (see chapter 2.2.2) to the NLO cross-section of $800\,\text{fb}^{+6.1}_{-7.4}\%$ [1].

As mentioned before in section 2.2.4 there are several different possible backgrounds, which must be considered in the analysis. The largest background for the dilepton channel is the Z+jets process. For the event generation and showering Sherpa 2.2.1 ([37], [38] and [39]) was used with nnpdf3.0NNLO [40] tuning. The second largest background is the $t\bar{t}$ background. It was simulated at NLO using the Powheg-Box event generator with CT10 [41] PDFs. The hadronisation was done using Pythia 6. The same method was used for the Wt background. The tWZ sample used nnpdf3.0 at NLO for its PDFs with a tune of A14 [42]. The used NLO generator was MadGraph 5_aMC@NLO with the showering done by Pythia 8. For the diboson samples WW, WZ and ZZ Sherpa 2.1.1 was used with CT10 PDFs at LO. Due to the low cross-section of gluon-induced processes compared to quark-induced ones [1] and the generally low impact of the diboson sample in the dilepton channel, gluon-induced processes were excluded. Finally for the $t\bar{t}$ pair production associated with a boson the nnpdf2.3 at LO PDFs were used with the A14 tuning parameters. For the event generators MadGraph 5_aMC@NLO 2.2.2 (for $t\bar{t}+W$) and MadGraph 5_aMC@NLO 2.2.3 (for $t\bar{t}+Z$ and $t\bar{t}+H$) were used. Fragmentation and hadronisation was once again done by Pythia 8. A table summarising the information can be found in the appendix (table B.1).

CHAPTER 5

Signal and background separation

5.1 Event selection

As already discussed in section 2.2 for the dilepton channel the Z-boson must decay into a lepton pair. In addition the top quark must first decay into a W-boson and a b-quark. The W-boson must then further decay into a quark pair. Accordingly two leptons and four quarks are expected. One of the four quarks must be a b-quark. The corresponding Feynman diagram can be found in 2.9.

In order to reach the highest signal/background ratio possible, cuts are applied to the samples. Only events with exactly two leptons of opposite sign and same flavour are selected. They must have an $|\eta| < 2.5$ due to detector limitations. In addition, four jets out of which one must have a b-tagging at 70 % working point are required with $|\eta| < 4.5$. In the case of the b-tagged jet, $|\eta|$ must be smaller than 2.5 since b-tagging is only available for central values of $|\eta|$. The Z+jets background is by far the largest background. Accordingly, the b-jet working point was optimised in order to differentiate between Z+jets and signal events. Since the Z+jets consists in large parts of events with no or more than one b-quark involved, the cut on exactly one b-jet improves the signal/background ratio significantly. Accordingly the tightest available working point of 70 % was chosen. In addition no other jet may be b-tagged, even at a working point of 85 %. Since the backgrounds, especially Z+jets, can have different momentum distributions for the different particles involved, the p_{T} cuts were optimised for signal/background separation. All particles are sorted according to their respective transverse momentum. The leading lepton must have a $p_{\mathrm{T}}^{\ell 1} > 28\,\mathrm{GeV}$ and the second lepton a $p_{\mathrm{T}}^{\ell 2} > 20\,\mathrm{GeV}$. For the first jet a lower limit for the $p_{\mathrm{T}}^{\mathrm{j1}}$ of 50 GeV is set in order to decrease the number of Z+jets background events. All other jets must fulfil $p_{\mathrm{T}}^{\mathrm{j2,\,j3,\,j4}} > 30\,\mathrm{GeV}$ (see table 5.1).

In addition to these, cuts on further reconstructed objects are also used to reduce the amount of background. The two leptons are combined to form the reconstructed Z boson. For the event to be considered the invariant mass of the reconstructed Z must be within a 20 GeV window of the actual Z-boson mass of roughly 91 GeV [6]. In the case of the W boson, the two not b-tagged jets with a mass closest to the W-boson mass are chosen. Together with the b-tagged jet they form the top quark. Its mass must lie within a 100 GeV window of the actual top-quark mass of roughly 172 GeV [6]. The remaining jet is then identified as the forward jet[1].

The p_{T} and η distributions of the jet and the lepton with the highest p_{T} can be found in figures 5.1, 5.2, 5.3 and 5.4. It can be confirmed by eye that the main contribution to the observed events is the Z+jets background. In addition it can also seen that the number of observed events is

[1] A forward jet is a jet with an $\eta > 3$.

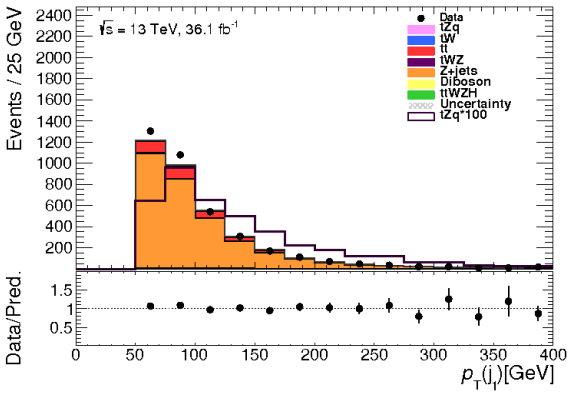

Figure 5.1: p_{T} distribution of the jet with the highest p_{T}.

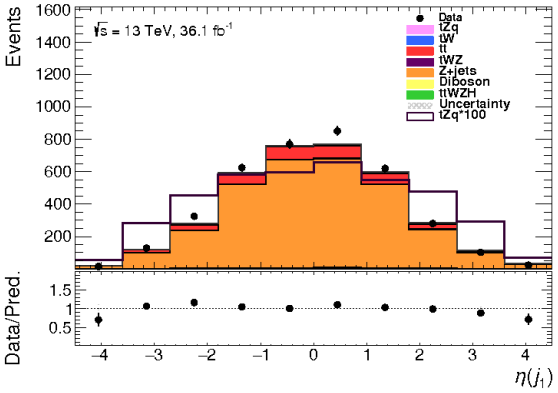

Figure 5.2: η distribution of the jet with the highest p_{T}.

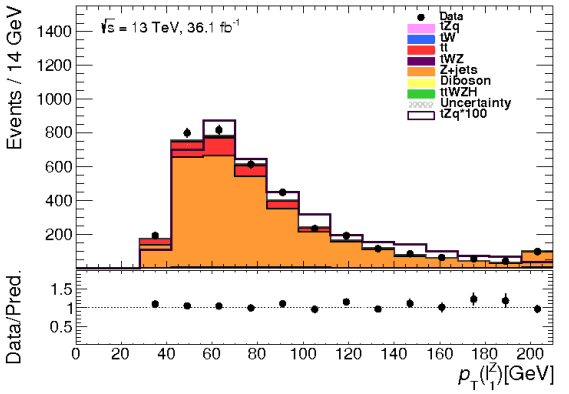

Figure 5.3: p_{T} distribution of the lepton with the highest p_{T}.

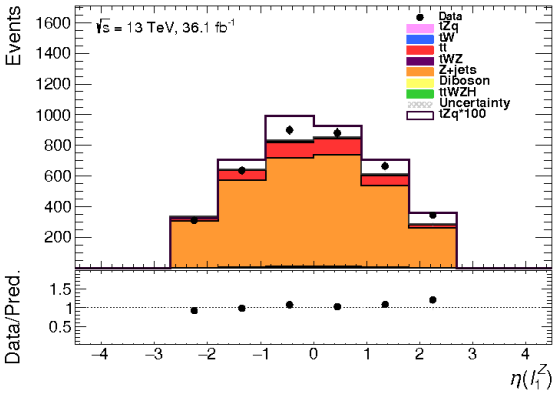

Figure 5.4: η distribution of the lepton with the highest p_{T}.

somewhat higher than the number of simulated events. In table 5.2 the number of events for the different Monte Carlo samples and the data are given. There is an about 8 % difference between the simulated and observed number of events. However due to comparatively large uncertainties on the Monte Carlo modelling of the Z+jets background (see section 6.1) this disagreement is acceptable.

The number of background events exceeds the number of signal events roughly by a factor of 100. No single variable offers enough discrimination power to drastically improve the ratio. Accordingly it is at this point difficult to gain any information concerning the signal from the data. In order to improve the signal/background separation a multivariate analysis is employed in the next step.

5.2 Multivariate analysis

5.2.1 General introduction

This introduction into multivariate analysis techniques is based on Ref. [43]. In the case of the cuts described above the values of single variables decide whether an event is dismissed as most likely

	No.	p_T	$\lvert\eta\rvert$	other
leptons	2	$p_T^{\ell 1} > 28\,\text{GeV}$, $p_T^{\ell 2} > 20\,\text{GeV}$	< 2.5	same flavour, opposite sign pair
Jets	4	$> 30\,\text{GeV}$, $p_T^{j1} > 50\,\text{GeV}$	< 4.5	
b-jet	1	$> 30\,\text{GeV}$	< 2.5	70 % b-tagging, add. veto at 85 %
$81\,\text{GeV} < m_{\ell\ell} < 101\,\text{GeV}$				
$122\,\text{GeV} < m_{bjj} < 222\,\text{GeV}$				

Table 5.1: Event selection applied for selecting events with a dileptonic final state.

Process	Number of events
Z+jets	3 099.5 ± 47.4
$t\bar{t}$	380.1 ± 11.6
$t\bar{t} + W/Z/H$	21.3 ± 0.3
Wt	13.8 ± 1.3
WW, WZ, ZZ	10.2 ± 1.5
tWZ	5.0 ± 0.3
tZq	40.2 ± 0.7
Total expected	3 570.1 ± 48.9
Data	3 737

Table 5.2: Number of events for the different MC backgrounds and the signal, as well as the observed data with the corresponding statistical uncertainties.

background or kept as a probable signal signal. Such a technique does not take into account the correlations between the different variables of an event. A multivariate analysis considers the full vector, $\boldsymbol{x}$, of variables of the event and combines its information into a single variable, γ. This variable γ can then be used to decide if the event is considered more background-like or signal-like. In order to combine the vector of variables into γ, machine learning – more specifically supervised machine learning – is used. Supervised learning uses events which are already identified as signal or background in order to teach the system how to differentiate between the two. In the case of high energy physics, Monte Carlo generated events are often used for the training as it is known for them whether an event is signal or background.

So called artificial neural networks are multivariate analysis techniques, which make the calculation of γ possible. The definition of γ may be chosen as:

$$\gamma(\boldsymbol{x}) = w_0 + \sum_{m=1}^{M} w_m \cdot h_m(\boldsymbol{x}) \tag{5.1}$$

with w_m being weights and $h_m(\boldsymbol{x})$ different basis functions. The dimension, M, may be chosen freely to optimise the results. The weights, $w_{0,m}$, are what the training should determine. This is done by defining and minimising a loss function. One example of a loss function is the squared loss:

$$L(w) = \sum_{i=0}^{\text{tot}} \left[\gamma_{\text{known}}^{(i)} - \gamma(\boldsymbol{x}^i; \boldsymbol{w})\right]^2 . \tag{5.2}$$

The $\gamma_{\text{known}}^{(i)}$ gives the known type of event i of the Monte Carlo sample, for example +1 for signal and −1 for background events. On the other hand $\gamma(\boldsymbol{x}^i; \boldsymbol{w})$ gives the calculated γ for the event i with weight

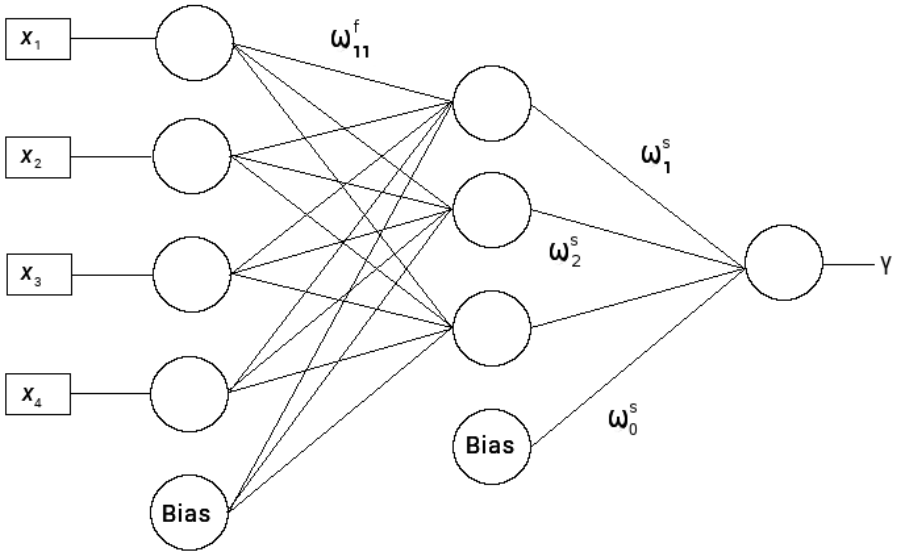

Figure 5.5: Graphical representation of a feed-forward neural network.

vector $\boldsymbol{w}$. The total number of Monte Carlo events used for the training is tot. Minimizing the function L gives then the best $\boldsymbol{w}$ for separating signal from background. Most of the time much more complicated loss functions are used and the starting weights are randomly chosen. They are then iteratively adjusted until a minimum is reached. This procedure is called backpropagation. The adjustments can for example be made using the derivative of the loss function and adjusting each weight by the corresponding value $\boldsymbol{w} \to \boldsymbol{w} + \eta \cdot \Delta_{\boldsymbol{w}}$. The learning rate, η, decides how quickly adjustments to the weights are made.

Instead of using M different basis functions, h_m, it is also possible to transform the function for γ:

$$\gamma(x) = w_0^s + \sum_{m=1}^{M} \left[w_m^s \cdot h \left(w_{0,m}^f + \sum_{k=1}^{D} w_{k,m}^f x_k \right) \right]. \tag{5.3}$$

The dimension, D, is the total number of variables used and w^f and w^s the first and second set of weights. The basis function, h, can then be freely chosen, depending on the properties of the samples analysed. A typical function used as basis function is the sigmoid function:

$$h(t) = \frac{1}{1 + e^{-t}}. \tag{5.4}$$

An example of a graphical representation of the process can be found in figure 5.5. The sum over k with the weights $w_{k,m}^f$ corresponds to the input layer with $D = 4$ nodes in this example. This means that four variables are available to the network. The second, so called hidden layer corresponds to the sum over the dimension $M = 3$ with weights w_m^s. This finally leads to the final layer which gives out γ. This specific design of a neural network is called a feed-forward artificial neural network, since it does not allow for feedback loops into previous layers. The bias nodes represent the weights w_0^f and w_0^s.

5.2.2 The NeuroBayes Package

The following information concerning the NeuroBayes Package is based on Ref. [44] and Ref. [45]. After the general introduction in the previous section, the NeuroBayes Package is explained in detail now. It is

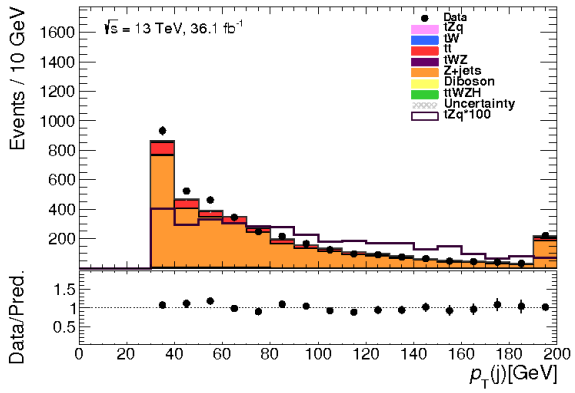

Figure 5.6: Stack plot of the p_T distribution of the forward jet.

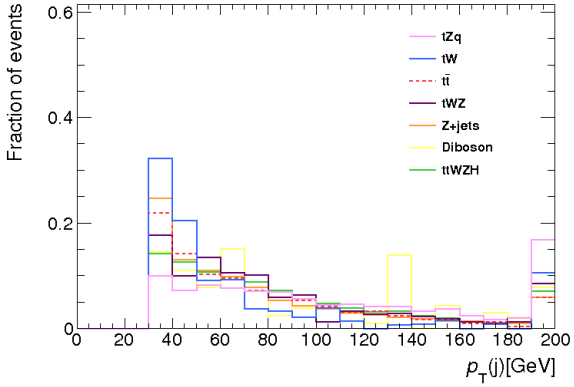

Figure 5.7: Overlay plot of the p_T distribution of the forward jet.

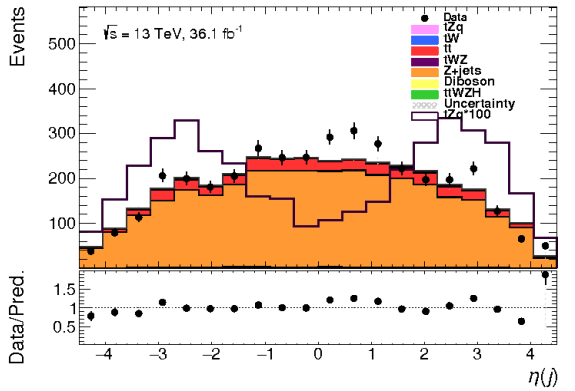

Figure 5.8: Stack plot of the η distribution of the forward jet.

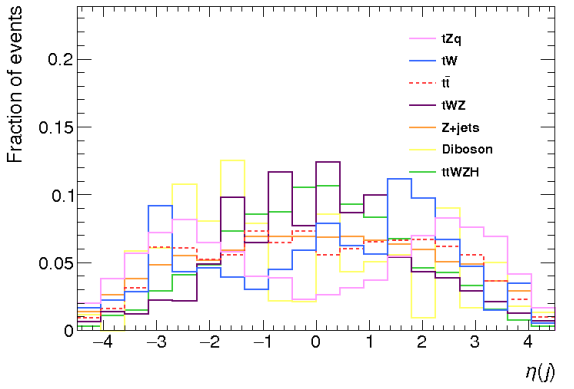

Figure 5.9: Overlay plot of the η distribution of the forward jet.

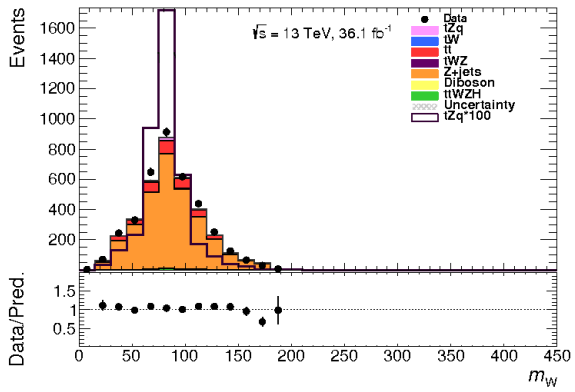

Figure 5.10: Stack plot of the reconstructed W-boson mass.

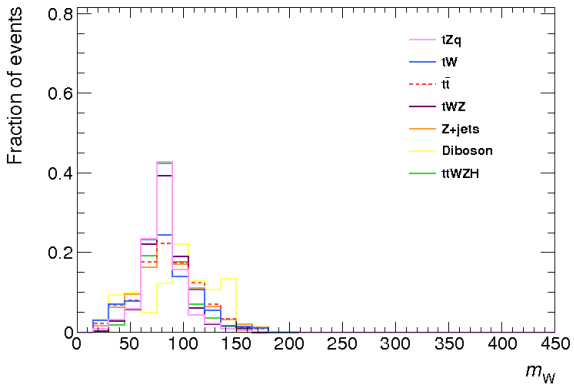

Figure 5.11: Overlay plot of the reconstructed W-boson mass.

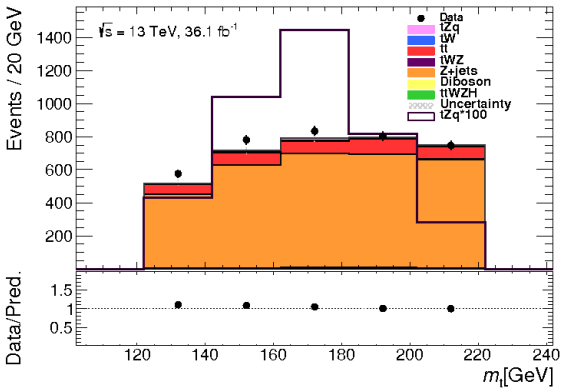

Figure 5.12: Stack plot of the reconstructed top-quark mass.

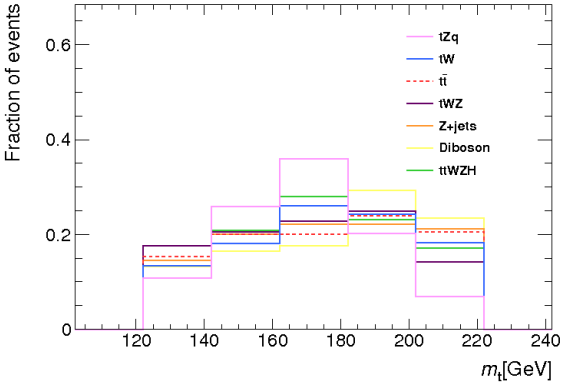

Figure 5.13: Overlay plot of the reconstructed top-quark mass.

a three layer feed-forward neural network, which is combined with an automated preprocessing structure. In the preprocessing for this analysis the different input variables are transformed from probability density functions to flat distributions to avoid network-related constrictions. Next they are transformed to Gaussian distributions. Afterwards the different variables are ranked according to their importance for the differentiation. For the ranking in this analysis the different variables are decorrelated and normalised. First the correlation matrix is computed. One variable at a time is removed from the the input list of variables and the correlation between it and the other variables is computed giving out a correlation matrix. Afterwards it is returned and the next variables is studied. In addition to computing the correlation matrix the variables are ranked according to their contribution to the total significance of the signal background separation. For this, the set-up calculates the loss of total significance when a single variable is removed - the so called additional significance. This is done for all variables and in the end the variable with the lowest additional significance is removed. The process is repeated until all variables are removed. Afterwards a list is made of all of them, which is sorted accordingly to their order of removal. All variables below a set additional significance are dismissed. In this analysis the variables must have a significance of at least $4\,\sigma$ to be included. This leads to a total of 11 included variables, which are listed in table 5.3. The correlation between the variables can lead to counter-intuitive effects: it is possible for a variable of higher additional significance to be ranked below one of lower additional significance. The higher ranked variable gained a high significance through the combination with other variables. Once these other variables are taken out of the consideration it loses most of its influence. For this analysis especially the p_{T} of the forward jet (see figure 5.8) as well as its η distribution (see figure 5.9) have a large impact on the separation of signal and background. This is due to the t-channel topology, which has a high probability of creating forward jets. In addition the reconstructed mass of the W boson (see figure 5.12) and the top quark influence the separation significantly (see figure 5.13). This is the case, since for most of the backgrounds such objects are not expected. Accordingly there is no peak expected for the regions of the particles' masses. Further plots can be found in the appendix C. 8 hidden nodes are used for the training.

For the training there are several different loss functions possible. The one chosen for this analysis is the entropy loss function. A Bayesian regularisation scheme is employed to avoid overfitting. Its γ is defined as

$$\gamma(x) = h\left[\sum_{m=1}^{M} w^s \cdot h\left(\sum_{k=1}^{D} w^f_{k,m} x_k\right)\right] \tag{5.5}$$

Variable	S ignificance(σ)	Definition
$p_{\mathrm{T}}^{\mathrm{j,forward}}$	25.4	p_{T} of the jet identified as the forward jet
$\eta_{\mathrm{j,forward}}$	24.9	η of the jet identified as the forward jet
m_W	24.8	mass of the reconstructed W boson
m_t	11.2	mass of the reconstructed top-quark
$p_{\mathrm{T}}^{W,\mathrm{j1}}$	9.3	p_{T} of the highest p_{T} jet associated to the W boson
$p_{\mathrm{T}}^{b\mathrm{j}}$	9.4	p_{T} of the b-tagged jet
$p_{\mathrm{T}}^{W,\mathrm{j2}}$	6.5	p_{T} of the second jet associated to the W boson
m_Z	5.6	mass of the reconstructed Z boson
$E_{\mathrm{T}}^{\mathrm{miss}}$	4.9	missing transverse energy
$\Delta\phi_{W,b}$	4.1	$\Delta\phi$ between the W boson and the b-jet
$\Delta\mathrm{R}_{W,b}$	4.5	ΔR between the W boson and the b-jet

Table 5.3: Variables used as input to the neural network ordered by their importance.

and h is the symmetric sigmoid function [46]:

$$h(t) = \frac{2}{1 + e^{-t}} - 1. \tag{5.6}$$

After training the NeuroBayes package provides several plots to judge the success of the training such as the correlation matrix, a signal purity plot or a signal efficiency vs. efficiency plot. The signal purity plot can be seen in figure 5.14. The purity, P, is defined as the number of signal events over the total number of events. The values should follow a linear distribution in the case of proper training as it can be shown that in this case:

$$P = \frac{\gamma + 1}{2} \tag{5.7}$$

If this is not the case it hints towards a problem in the minimisation process of the error function. The final separation of signal and background can be found in figure 5.15. This plot shows the normalised distributions for the the signal sample and the background samples. For the training of the neural network all available backgrounds are trained against the signal sample. The output variable of the neural network is a continuous number between -1 and 1, with -1 containing mostly background events and 1 mostly signal events. Accordingly in the case of a successful training the background distribution will peak close to -1, while the signal distribution will peak close to 1.

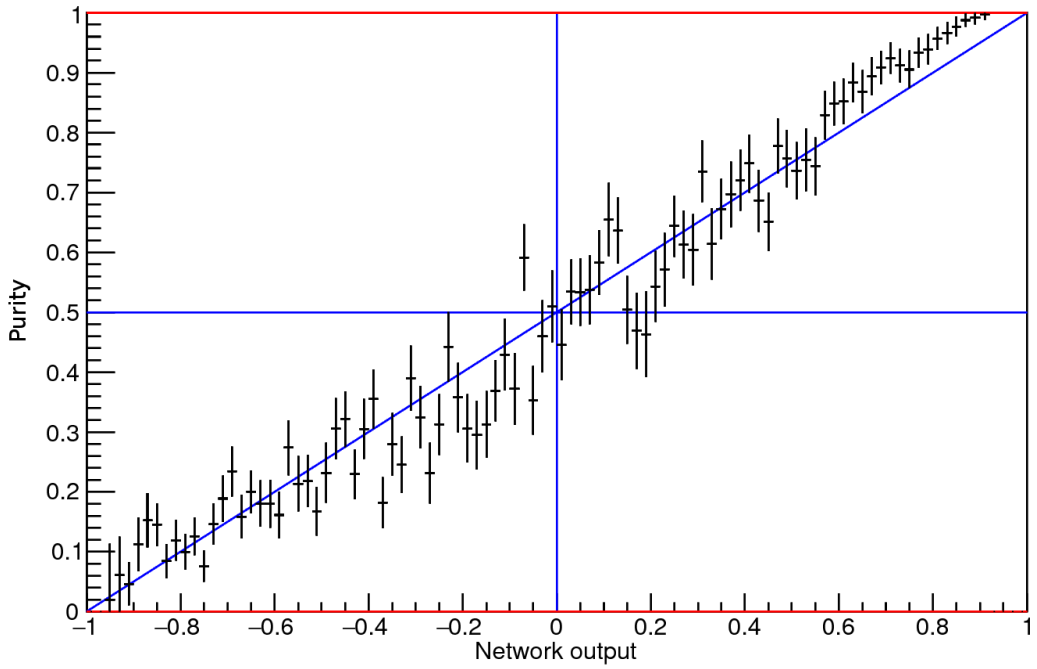

Figure 5.14: Signal purity dependent on the neural network output for the training of the neural network.

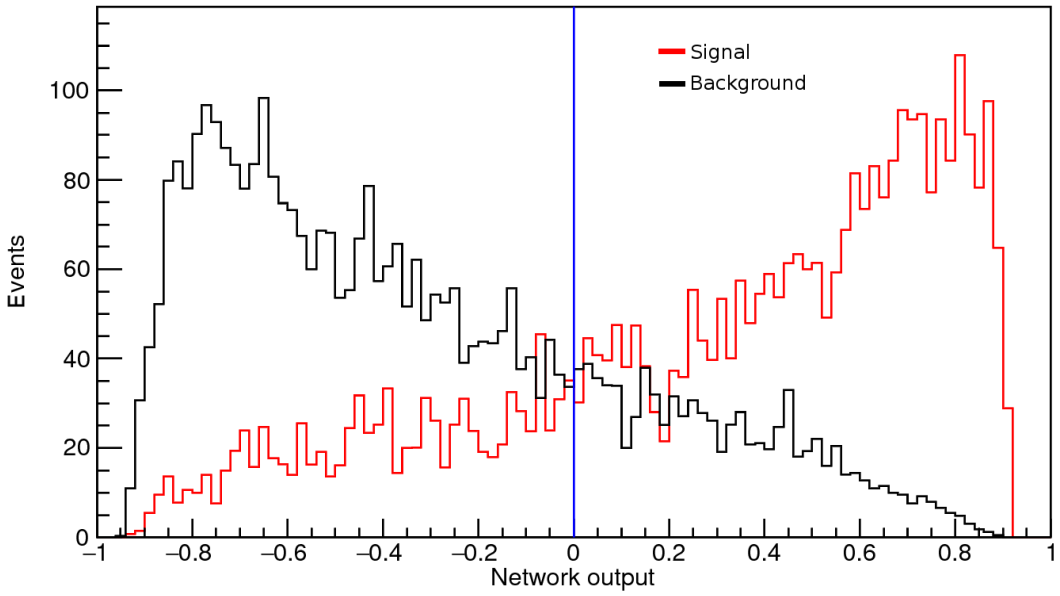

Figure 5.15: Signal background separation by the neural network with the output variable -1 being identified as containing mostly background events and 1 mostly signal events.

CHAPTER 6

Signal extraction

6.1 Systematic uncertainties

There are several different sources for systematic uncertainties which must be considered. First of all there are uncertainties related to the reconstruction efficiencies and the calibration of the detector. In addition there are uncertainties on the possibility of additional radiations. Finally there are uncertainties on the luminosity and the normalisation of the different backgrounds. The uncertainties included are introduced in the following and the impact on this analysis is discussed in section 6.3.

6.1.1 Reconstruction efficiency and calibration uncertainties

Jets

One of the largest contributions to the systematic uncertainties comes from the Jet Energy Scale (JES). The measured energy of the jets is not necessarily the same as the true energy of the particle. In fact in most instances the measured energy is below the true one. This is due to many different effects [47]:

- dead material in the detector
- differences in the scales of the hadronic and electromagnetic showers
- energy which is not included in the reconstructed jet as it is deposited outside of the jet cone
- energy deposits below the noise thresholds of the calorimeter
- pile-up

In order to counteract these effects a complex system is applied to rescale the measured jet energies. A set of uncertainties is estimated as well. The uncertainties are combined due to their large number. There are in total 88 uncertainties, which can be divided into 75 *in-situ* uncertainties and 13 additional other uncertainties. The 75 uncertainties are reduced to 8 by diagonalising the total covariance matrix of the JES correction factors. The new, reduced set of uncertainties are then derived from the eigenvectors and eigenvalues of the matrix [48]. This leads to in total 21 uncertainties, also called nuisance parameters (NPs).

Besides the scaling of the energy it is also necessary to consider the precision of the measurement – the Jet Energy Resolution (JER). The reason for a smearing of the distribution can for example be electronic noise and pile-up effects as well as stochastic effects, which come from the sampling nature of the calorimeters. The estimation of the JER is described in Ref. [47].

In addition to the JER and the JES there are further uncertainty sources related to jets. They correspond to the identification of the jet type, such as b-tagging which is used in this analysis. Both the uncertainties on the b-tagging as well as its efficiency must be taken into account. They are determined in Ref. [49] and Ref. [50] and adapted to the current detector set-up. The b-tagging scale factor considers that the b-tagging performance in data and simulation varies and corrects the b-tagging performance in simulation accordingly.

Leptons

Besides the uncertainties concerning jets there are of course also uncertainties related to the leptons. Similar to the jets there are uncertainties on the energy scale, resolution and particle identification. Finally there are uncertainties on the trigger. The energy scale and resolution for leptons is calculated separately for electrons and muons. $Z \rightarrow ll$ decays are used to set the energy scale. The details are described in Ref. [51] for electrons and in Ref. [24] for muons. They are calculated in Ref. [52] and Ref. [24].

Missing transverse energy

Finally the missing transverse energy ($E_{\mathrm{T}}^{\mathrm{miss}}$) has corresponding uncertainties. For Run~2 the preferred algorithm to quantify the $E_{\mathrm{T}}^{\mathrm{miss}}$ is the track-based soft term (TST) algorithm which combines a track-based method with a calorimeter based one [53]. In the case of the missing transverse energy it is necessary to differentiate between soft and hard events. While hard events correspond to identified physical objects such as jets, electrons or photons, soft events are not identified as such. They consist of charged particle tracks, which are not connected to a reconstructed physical object. As each of the reconstructed physical particles have uncertainties on the energy, these must be considered in the uncertainties of the $E_{\mathrm{T}}^{\mathrm{miss}}$. In addition the soft events also have uncertainties, which must be included. Their calculation is described in Ref. [53]. The calculated $E_{\mathrm{T}}^{\mathrm{miss}}$ has two assigned uncertainties: the energy resolution as well as its scale. For the energy resolution of the $E_{\mathrm{T}}^{\mathrm{miss}}$ the uncertainty is split into two parts: the total soft transverse momentum ($p_{\mathrm{T}}^{\mathrm{soft}}$) is projected onto the total hard transverse momentum ($p_{\mathrm{T}}^{\mathrm{hard}}$) and an uncertainty assigned for both the term parallel and the term perpendicular to the $p_{\mathrm{T}}^{\mathrm{hard}}$.

6.1.2 Radiation uncertainties

Due to higher order effects it is possible for gluons to be radiated from particles of both the initial and the final state. These radiations are taken into account by the radiation uncertainty. In order to estimate the effect of varying amounts of additional radiation in the signal Monte Carlo sample two additional samples are processed. While one sample contains events with a higher amount of radiation than predicted, the second sample contains events with a lower amount of radiation. The factorisation, renormalisation scale and the set of tuned parameters is varied accordingly. The resulting samples are then used to estimate the radiation uncertainty.

6.1.3 Luminosity and background uncertainties

The uncertainty on the luminosity is estimated to be 2.1 %. A method similar to the one described in Ref. [54] is applied to estimate it. In addition uncertainties on the background normalisations must also be included. The value of the uncertainty is dependent on the background. For the main background of Z+jets a normalisation uncertainty of 20 % is applied. This is conservatively estimated based on the study done in Ref. [55]. In said study different Monte Carlo event generators are used to measure the production cross-section of a Z-boson in association with jets. Their performance is compared for the different numbers of jets associated with the Z-boson. For four jets none of the event generators have a

data to Monte Carlo disagreement above 20 %. Accordingly an uncertainty of 20 % is chosen. In the case of $t\bar{t}$ it is estimated to be 5.5 % following the current ATLAS recommendation ([56] and [57]). The background of $t\bar{t}$ is combined with the Wt background for the fit. Since the influence of Wt is relatively small, the uncertainty of $t\bar{t}$ is applied to the combined sample. Finally the remaining backgrounds are combined in "Other". The uncertainty is set for 13 % based on Ref. [58].

6.2 Statistical analysis

The signal strength, μ, is defined as

$$\mu = \frac{\sigma_{\text{measured}}}{\sigma_{\text{predicted}}}. \tag{6.1}$$

In order to gain information concerning the signal strength an upper limit is computed using the software framework HistFitter [59]. It is widely used in ATLAS for statistical data analysis and performs binned likelihood fits as well as statistical interpretations of the results. In the case of this analysis HistFitter is used to compute an upper limit on the signal strength using a hypothesis test.

To test how well the measured data agrees with the Standard Model predictions, the hypothesis is made that the Standard Model prediction for tZq is correct, leading to a signal strength of $\mu = 1$. Said hypothesis must be tested, however it is not generally possible to give absolute answers such as "true" or "false". Instead it is only possible to give confidence levels or corresponding so called p-values. The p-value gives "the probability to obtain data at least as incompatible with the hypothesis as the present data if the hypothesis considered is actually true"(cited from Ref. [43]). In this case it is defined as

$$p_\mu = \int_{q_{\mu,\,\text{upperlimit}}}^{\infty} P(q_\mu|\mu) dq_\mu \tag{6.2}$$

The function $P(q_\mu|\mu)$ is a probability density function, which gives the probability that the so called test statistic, q_μ, is true for a given μ. The integral over a certain region of the test statistic then gives the p-value [60]. In the case of calculating the upper limit a p-value is set, for example $p \leq \alpha$ with $\alpha = 0.05$ and the corresponding $q_{\mu,\,\text{upperlimit}}$ is searched for by increasing $\mu_{\text{upperlimit}}$ until the p-value drops low enough [61]. Since the p-value corresponds to the confidence level, for example an $\alpha = 0.05$ corresponds to the confidence level of 95 % [61], it is then possible to give an upper limit, $\mu_{\text{upperlimit}}$, with a confidence level of 95 %. In the following the test statistic will be introduced in more detail.

In this analysis the information concerning the strength of the signal tZq must be drawn from the measured data events by using the simulated Monte Carlo samples. The strength of the signal sample, μ, is to be constrained by an upper limit and is accordingly unknown. It is multiplied by the simulated number of signal events to get the mean expected number of events, $\nu(\mu)$. The probability of observing a certain number of events, n, in the case of a given $\nu(\mu)$ is described by the Poisson distribution, a probability density function [43]:

$$f(n;\nu(\mu)) = \frac{\nu^n}{n!} \cdot e^{-\nu} \tag{6.3}$$

In the case of statistically independent measurements, which is the case for different bins of one measurement, the probability density functions, $f(n_i;\nu_i)$, can be combined by the likelihood function:

$$L(\boldsymbol{n},\mu) = \prod_{i=1}^{\text{Bins}} f(n_i;\nu_i(\mu)) \tag{6.4}$$

For the above equation the assumption was made that no uncertainties have to be considered. If an uncertainty, u, has to be included the likelihood function is extended by an additional term, G:

$$L(\boldsymbol{n}, \mu, \theta) = \prod_{i=1}^{N} f(n_i; \nu_i(\mu, u, \theta)) \cdot G_N(\theta; u) \tag{6.5}$$

The value u gives the uncertainty and θ a parameter which follows a normal distribution. The mean expected number of events is also dependent on the uncertainty, u, and its factor θ. Since the profile ratio of the likelihood function is a more powerful estimator than the function itself, it is used instead:

$$\lambda = \frac{L(\boldsymbol{n}, \mu, \hat{\hat{\theta}})}{L(\boldsymbol{n}, \hat{\mu}, \hat{\theta})} \tag{6.6}$$

Here $\hat{\hat{\theta}}$ is the value, which maximises L for a given μ and the corresponding $L(\boldsymbol{n}, \mu, \hat{\hat{\theta}})$ is called the conditional maximum likelihood function. The denominator is the unconditional maximum likelihood function with the estimators $\hat{\mu}$ and $\hat{\theta}$. They give the global maximum of L. The profile ratio is then used to calculate the test statistic, q_μ, which for upper limit calculations for Histfitter is:

$$q_\mu = \begin{cases} -2ln\lambda(\mu) & \text{for } \hat{\mu} < \mu, \\ 0 & \text{for } \hat{\mu} > \mu \end{cases} \tag{6.7}$$

Instead of using this test statistic, it is possible to estimate the function of q using the asymptotic calculator. The corresponding function can be found in Ref. [60].

With this test statistic and the method described above it is now possible to calculate the upper limit at a given confidence level. However it should be noted that in the case of low sensitivity of the data to the desired process, a model might be rejected, even though it should not. Accordingly the calculated upper limit may be anomalously low. In order to avoid this problem the CL_s method can be applied. In this case instead of requiring that $p_\mu \leq \alpha$, one requires that $CL_s \leq \alpha$, where CL_s is defined as [6]:

$$CL_s = \frac{p_\mu}{1 - p_b}. \tag{6.8}$$

Here p_b is the p-value of the background-only hypothesis – meaning that $\mu = 0$. Since for decreasing sensitivity the denominator $1 - p_b$ also decreases, the condition $CL_s \leq \alpha$ is less likely to be fulfilled.

Histfitter first performs several initial hypothesis tests using the asymptotic calculator and the CL_s method. Afterwards a second scan with smaller intervals uses the initial result to gain the final upper limit. This is done once with the measured data to gain the computed upper limit and once using Asimov data to gain the expected limit. Asimov data is in this case defined as the sum of all Monte Carlo samples normalised to their Standard Model expectations.

6.3 Fit results

For this analysis both the computed and expected upper limits are calculated at a 95 % confidence level.

There are several uncertainties, which have a large impact on the result. The impact of the uncertainties on the signal sample tZq is listed in table 6.1. The table does not include the background uncertainties. Especially the radiation uncertainty has a large influence on the tZq sample. The impact of the uncertainties on the upper limit calculation can be observed in figure 6.1. It displays two different sets of values.

Source	Uncertainty [%]
tZq radiation	±37.1
Jets	±4.7
b-tagging	±2.7
Luminosity	±2.1
MC statistics	±1.4
Leptons	±1.3

Table 6.1: Impact of the systematic uncertainties acting directly on the signal sample tZq.

channel	exp. events	fitted events
total	3 556±843	3 736±61
tZq	40±15	15^{+25}_{-15}
$t\bar{t} + Wt$	380±63	407±36
other	36±5	37±5
Z+jets	3 100±803	3 276±81

Table 6.2: Yields table before and after the fit. There are in total 3737 observed events.

While the upper scale is related to the black dots ("pull") with their bars ("constraint") the lower scale corresponds to the yellow and blue bars. Before the fit is executed the pull of each uncertainty has a value of 0 and the constraint spans within $\pm 1\sigma$. The fit is used to reduce the constraint and correct the value of the pull. The result is shown in the graph. The bars then give the corresponding impact on the signal significance both for the pre and post fit parameters. Here the normalisation of the Z+jets sample has the largest influence. Although the value is strongly constrained by the fit the $\frac{\Delta\mu}{\mu}$ ratio is still above 30 %. The next largest impact has a component of the JES: the JES flavour composition has a $\frac{\Delta\mu}{\mu}$ ratio of about 20 %. The tZq radiation as well as three additional JES components all follow with similar impacts. Though they are all somewhat constrained by the fit, the constraint is much lower than for the Z+jets normalisation. The fit compensated for the low number of Monte Carlo events by increasing the number of Z+jets background events significantly. The number of Z+jets events is increased by 6 %. The $t\bar{t} + Wt$ background is also increased by 7 %. This strong increase of background events can be explained by the fact, that too few Monte Carlo events are mainly observed at the two bins with the lowest neural network output variable (see figure 6.2). In these bins only very few signal events are expected, making it unlikely that a scaling of the signal would improve the situation. Different from the background events, the signal events of tZq are actually significantly decreased by the fit to only 15 events. Overall the data/Monte Carlo agreement is greatly improved by the fit (see figure 6.3). While before the predicted total number of events was only 3556 with a very high uncertainty of 843, the fit increases the total number of predicted events to 3736 with only 61 events uncertainty. As expected for a likelihood fit, it matches well with the observed 3737 events (see table 6.2).

The expected upper limit of the signal strength is 2.9. The computed upper limit of the signal strength is 5.3. Considering the small signal background ratio, the result is satisfactory. In appendix A considerations for possible future directions and improvements are made.

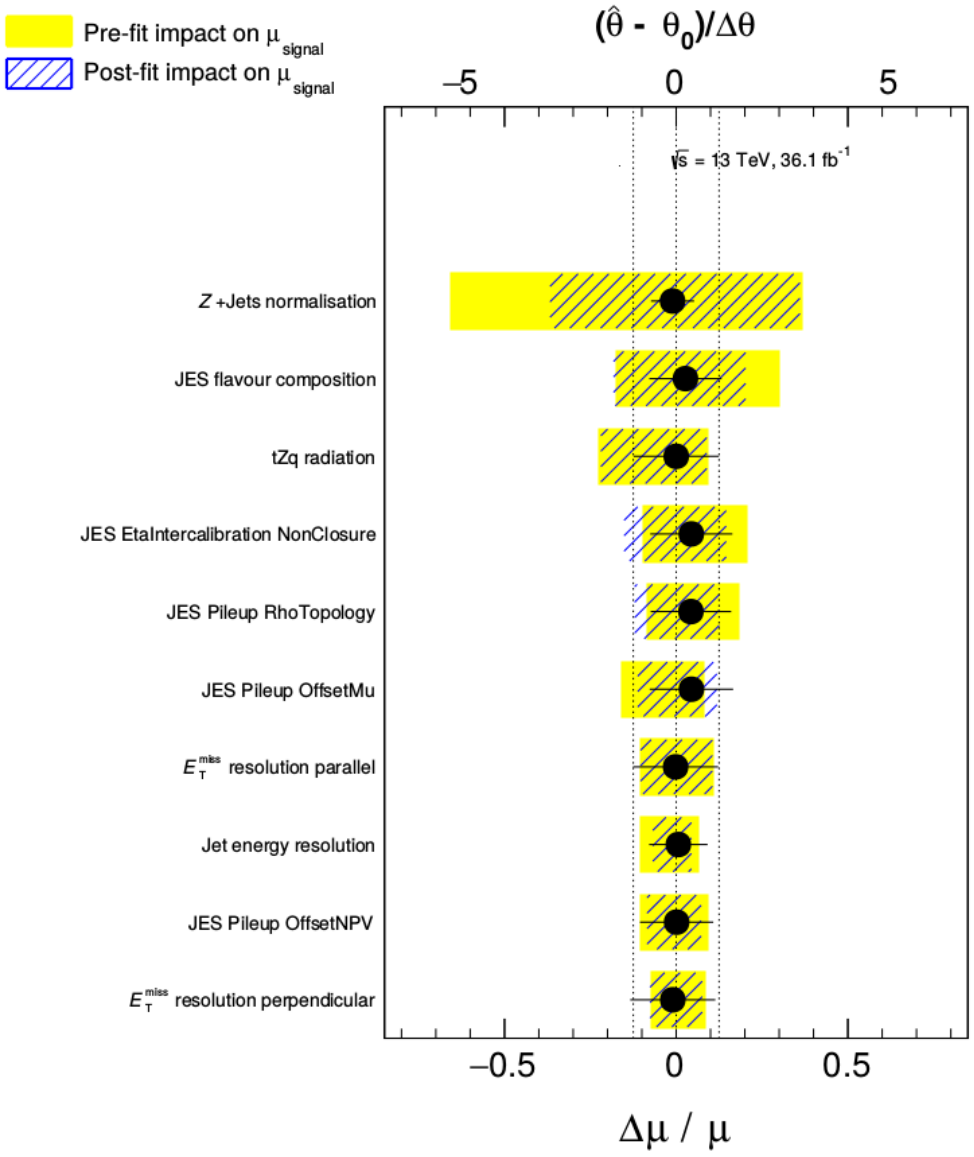

Figure 6.1: Summary of the 10 dominating uncertainties, ranked by their impact on the signal strength parameter.

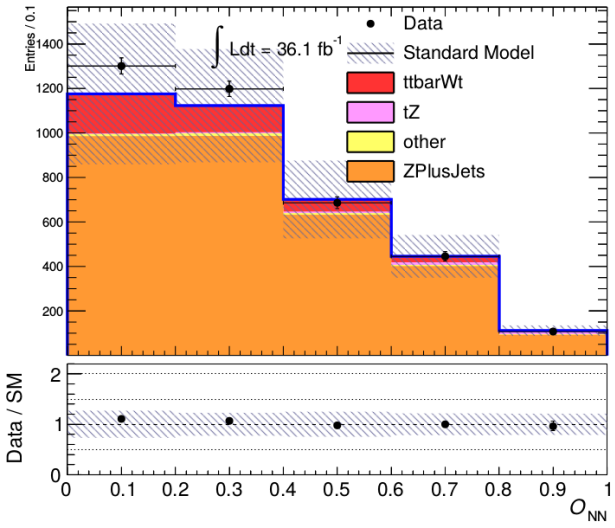

Figure 6.2: Data/Monte Carlo comparison of the neural network output distribution before the fit.

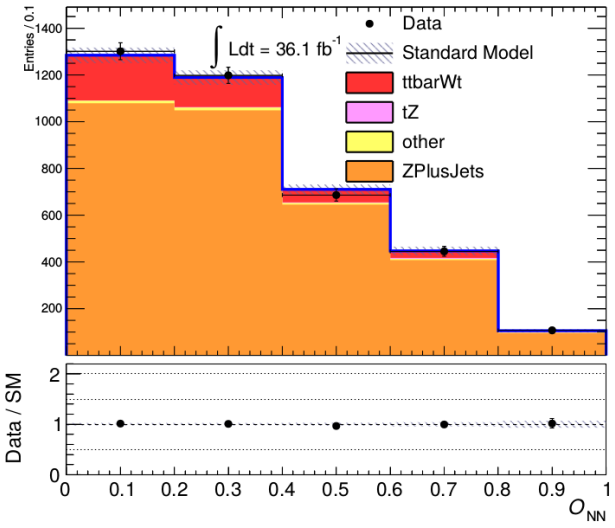

Figure 6.3: Data/Monte Carlo comparison of the neural network output distribution after the fit.

CHAPTER 7

Conclusion

In this thesis the single top quark production in association with a Z boson was studied in the dileptonic decay channel. In this channel the Z boson decays into a pair of charged leptons, while the top quark decays into a b-quark and a W boson and the W boson then decays hadronically. The event selection was optimised using Monte Carlo simulated samples to maximise signal and background separation. However, the larger cross-section and very similar final state of the main background, Z+jets, led to about a factor of 100 more background than signal events after selection. In order to improve the separation, a multivariate analysis – a neural network – was employed. The neural network combines all of the kinematic variables into a single discriminating one. The network was trained with Monte Carlo samples of all of the considered backgrounds, along with the signal sample of tZq. An upper limit binned likelihood hypothesis test was then performed to extract an upper limit on the theory prediction of the tZq cross-section. Different systematic uncertainties were included in the fit: besides uncertainties due to the experimental limitations of the detector, such as the reconstruction efficiencies and the calibration of the detector, the uncertainties on the theory predictions and the luminosity were also included. Finally the uncertainties on the normalisation of the different backgrounds was considered. Two additional studies concerning possible improvements and future directions were also made.

This is the first complete study of the dilepton final state done at ATLAS. The expected upper limit on the signal strength, μ, is 2.9. The computed upper limit is somewhat looser at 5.9.

Bibliography

[1] *Measurement of the production cross-section of a single top quark in association with a Z boson in proton–proton collisions at 13 TeV with the ATLAS detector*, tech. rep. ATLAS-CONF-2017-052, CERN, 2017, URL: https://cds.cern.ch/record/2273868 (cit. on pp. 1, 8, 21).

[2] M. Thomson, *Modern Particle Physics*, 1st ed., Cambridge University Press, 2013 (cit. on pp. 3, 5, 6).

[3] D. Griffiths, *Introduction to Elementary Particles*, 2nd ed., Wiley-VCH, 2008 (cit. on pp. 3, 5–7).

[4] I. Brock and T. Schörner-Sadenius, *Physics at the Terascale*, 1st ed., Wiley-VCH, 2011 (cit. on p. 3).

[5] T. Liss, F. Maltoni and A. Quadt, *The Top Quark*, http://pdg.lbl.gov/2017/reviews/rpp2016-rev-top-quark.pdf, [Online; accessed 2017-08-17], 2015 (cit. on p. 3).

[6] K. A. Olive et al., *Review of Particle Physics*, Chin. Phys. **C38** (2014) 090001 (cit. on pp. 4–7, 9, 23, 34, 50).

[7] ATLAS and CMS Collaborations, *Combined Measurement of the Higgs Boson Mass in pp Collisions at $\sqrt{s}$ = 7 and 8 TeV with the ATLAS and CMS Experiments*, Phys. Rev. Lett. **114** (2015) 191803, arXiv: 1503.07589 [hep-ex] (cit. on p. 5).

[8] J. Stillings, *Search of the associated production of a W boson and a top quark with the ATLAS detector at 7 TeV*, PhD thesis: Physikalisches Institut der Universität Bonn, 2015 (cit. on p. 7).

[9] ATLAS collaboration, *Measurement of the inclusive cross-sections of single top-quark and top-antiquark t-channel production in pp collisions at $\sqrt{s}$ = 13 TeV with the ATLAS detector*, JHEP **04** (2017) 086, arXiv: 1609.03920 [hep-ex] (cit. on p. 8).

[10] "LHC Guide", 2017, URL: http://cds.cern.ch/record/2255762 (cit. on p. 11).

[11] ATLAS collaboration, *The ATLAS Experiment at the CERN Large Hadron Collider*, JINST **3** (2008) S08003 (cit. on pp. 11, 14, 15, 17).

[12] M. Dosanjh, *From Particle Physics to Medical Applications*, 2399-2891, IOP Publishing, 2017, ISBN: 978-0-7503-1444-2, URL: http://dx.doi.org/10.1088/978-0-7503-1444-2ch1 (cit. on p. 12).

[13] I. Brock, *Particle Collision and Detection*, http://stanford.edu/group/stanford_atlas/4Particle%20Collision%20and%20Detection, [Online; accessed 2017-08-17] (cit. on p. 14).

[14] M. Schott and M. Dunford, *Review of single vector boson production in pp collisions at $\sqrt{s}$ = 7 TeV*, Eur. Phys. J. **C74** (2014) 2916, arXiv: 1405.1160 [hep-ex] (cit. on p. 15).

[15] S. Mergelmeyer, *Measurement of the Associated Production of a Single Top Quark and a W Boson in Single-Lepton Events with the ATLAS Detector*,
PhD thesis: Physikalisches Institut der Universität Bonn, 2015 (cit. on p. 16).

[16] ATLAS collaboration,
Expected Performance of the ATLAS Experiment - Detector, Trigger and Physics, (2009),
arXiv: 0901.0512 [hep-ex] (cit. on p. 16).

[17] G. Mullier,
The upgraded Pixel Detector of the ATLAS experiment for Run-2 at the Large Hadron Collider,
Journal of Instrumentation **11** (2016) C02061,
URL: http://stacks.iop.org/1748-0221/11/i=02/a=C02061 (cit. on p. 16).

[18] ATLAS collaboration, *ATLAS inner detector: Technical Design Report, 1*,
Technical Design Report ATLAS, CERN, 1997, URL: https://cds.cern.ch/record/331063
(cit. on p. 16).

[19] ATLAS collaboration, *ATLAS detector and physics performance: Technical Design Report, 1*,
Technical Design Report ATLAS, CERN, 1999, URL: https://cds.cern.ch/record/391176
(cit. on p. 18).

[20] A. R. Martínez, *The Run-2 ATLAS Trigger System*, J. Phys. Conf. Ser. **762** (2016) 012003
(cit. on p. 18).

[21] ATLAS collaboration, *Performance of the ATLAS Trigger System in 2015*,
Eur. Phys. J. **C77** (2017) 317, arXiv: 1611.09661 [hep-ex] (cit. on p. 18).

[22] ATLAS collaboration, *Electron efficiency measurements with the ATLAS detector using the 2012 LHC proton-proton collision data*, tech. rep. ATLAS-CONF-2014-032, CERN, 2014,
URL: http://cds.cern.ch/record/1706245 (cit. on p. 19).

[23] ATLAS collaboration, *Electron efficiency measurements with the ATLAS detector using the 2015 LHC proton-proton collision data*, tech. rep. ATLAS-CONF-2016-024, CERN, 2016,
URL: http://cds.cern.ch/record/2157687 (cit. on p. 19).

[24] ATLAS collaboration, *Muon reconstruction performance of the ATLAS detector in proton–proton collision data at* $\sqrt{s}$ *=13 TeV*, Eur. Phys. J. **C76** (2016) 292, arXiv: 1603.05598 [hep-ex]
(cit. on pp. 20, 32).

[25] M. Cacciari and G. P. Salam, *Dispelling the* N^3 *myth for the* k_t *jet-finder*,
Phys. Lett. **B641** (2006) 57, arXiv: hep-ph/0512210 [hep-ph] (cit. on p. 20).

[26] M. Cacciari, G. P. Salam and G. Soyez, *The Anti-k(t) jet clustering algorithm*,
JHEP **04** (2008) 063, arXiv: 0802.1189 [hep-ph] (cit. on p. 20).

[27] ATLAS collaboration, *Jet energy measurement and its systematic uncertainty in proton-proton collisions at* $\sqrt{s}$ = 7 *TeV with the ATLAS detector*, Eur. Phys. J. **C75** (2015) 17,
arXiv: 1406.0076 [hep-ex] (cit. on p. 20).

[28] ATLAS collaboration, *Performance of pile-up mitigation techniques for jets in pp collisions at* $\sqrt{s}$ = 8 *TeV using the ATLAS detector*, Eur. Phys. J. **C76** (2016) 581,
arXiv: 1510.03823 [hep-ex] (cit. on p. 20).

[29] ATLAS collaboration, *Performance of b-Jet Identification in the ATLAS Experiment*,
JINST **11** (2016) P04008, arXiv: 1512.01094 [hep-ex] (cit. on p. 20).

[30] ATLAS collaboration, *Performance of the ATLAS Trigger System in 2015*, Eur. Phys. J. **C77** (2017) 317, arXiv: 1611.09661 [hep-ex] (cit. on p. 20).

[31] ATLAS collaboration, *Trigger Menu in 2016*, tech. rep. ATL-DAQ-PUB-2017-001, CERN, 2017, URL: https://cds.cern.ch/record/2242069 (cit. on p. 20).

[32] S. Agostinelli et al., *Geant4—a simulation toolkit*, Nuclear Instruments and Methods in Physics Research Section A: Accelerators, Spectrometers, Detectors and Associated Equipment **506** (2003) 250, ISSN: 0168-9002, URL: http://www.sciencedirect.com/science/article/pii/S0168900203013688 (cit. on p. 21).

[33] J. Pumplin et al., *New generation of parton distributions with uncertainties from global QCD analysis*, JHEP **07** (2002) 012, arXiv: hep-ph/0201195 [hep-ph] (cit. on p. 21).

[34] J. Alwall et al., *The automated computation of tree-level and next-to-leading order differential cross sections, and their matching to parton shower simulations*, JHEP **07** (2014) 079, arXiv: 1405.0301 [hep-ph] (cit. on p. 21).

[35] T. Sjostrand, S. Mrenna and P. Z. Skands, *PYTHIA 6.4 Physics and Manual*, JHEP **05** (2006) 026, arXiv: hep-ph/0603175 [hep-ph] (cit. on p. 21).

[36] P. Z. Skands, *Tuning Monte Carlo Generators: The Perugia Tunes*, Phys. Rev. **D82** (2010) 074018, arXiv: 1005.3457 [hep-ph] (cit. on p. 21).

[37] T. Gleisberg et al., *Event generation with SHERPA 1.1*, JHEP **02** (2009) 007, arXiv: 0811.4622 [hep-ph] (cit. on p. 21).

[38] E. Bothmann, M. Schönherr and S. Schumann, *Reweighting QCD matrix-element and parton-shower calculations*, Eur. Phys. J. **C76** (2016) 590, arXiv: 1606.08753 [hep-ph] (cit. on p. 21).

[39] S. Kallweit et al., *NLO QCD+EW predictions for V + jets including off-shell vector-boson decays and multijet merging*, JHEP **04** (2016) 021, arXiv: 1511.08692 [hep-ph] (cit. on p. 21).

[40] R. D. Ball et al., *Parton distributions for the LHC Run II*, JHEP **04** (2015) 040, arXiv: 1410.8849 [hep-ph] (cit. on p. 21).

[41] H.-L. Lai et al., *New parton distributions for collider physics*, Phys. Rev. **D82** (2010) 074024, arXiv: 1007.2241 [hep-ph] (cit. on p. 21).

[42] ATLAS collaboration, *ATLAS Run 1 Pythia8 tunes*, tech. rep. ATL-PHYS-PUB-2014-021, CERN, 2014, URL: https://cds.cern.ch/record/1966419 (cit. on p. 21).

[43] O. Behnke et al., *Data Analysis in High Energy Physics: A Practical Guide to Statistical Methods*, 1st, Wiley-VCH, 2013 (cit. on pp. 24, 33).

[44] M. Feindt and U. Kerzel, *The NeuroBayes NeuralNetwork Package*, http://www-ekp.physik.uni-karlsruhe.de/~feindt/acat05-neurobayes, [Online; accessed 2017-08-22] (cit. on p. 26).

[45] <phi-t> Physics Information Technology, *The NeuroBayes User's Guide*, [Version 2010-04-06] (cit. on p. 26).

[46] M. Feindt, *A Neural Bayesian Estimator for Conditional Probability Densities*, (2004), arXiv: physics/0402093 [physics.data-an] (cit. on p. 29).

[47] ATLAS collaboration, *Monte Carlo Calibration and Combination of In-situ Measurements of Jet Energy Scale, Jet Energy Resolution and Jet Mass in ATLAS*, tech. rep. ATLAS-CONF-2015-037, CERN, 2015, URL: http://cds.cern.ch/record/2044941 (cit. on p. 31).

[48] ATLAS collaboration, *Jet energy measurement and its systematic uncertainty in proton-proton collisions at $\sqrt{s}$ = 7 TeV with the ATLAS detector*, Eur. Phys. J. **C75** (2015) 17, arXiv: 1406.0076 [hep-ex] (cit. on p. 31).

[49] ATLAS collaboration, *Calibration of the performance of b-tagging for c and light-flavour jets in the 2012 ATLAS data*, tech. rep. ATLAS-CONF-2014-046, CERN, 2014, URL: https://cds.cern.ch/record/1741020 (cit. on p. 32).

[50] ATLAS collaboration, *Calibration of b-tagging using dileptonic top pair events in a combinatorial likelihood approach with the ATLAS experiment*, tech. rep. ATLAS-CONF-2014-004, CERN, 2014, URL: https://cds.cern.ch/record/1664335 (cit. on p. 32).

[51] ATLAS collaboration, *Electron and photon energy calibration with the ATLAS detector using LHC Run 1 data*, Eur. Phys. J. **C74** (2014) 3071, arXiv: 1407.5063 [hep-ex] (cit. on p. 32).

[52] ATLAS collaboration, *Electron identification measurements in ATLAS using $\sqrt{s}$ = 13 TeV data with 50 ns bunch spacing*, tech. rep. ATL-PHYS-PUB-2015-041, CERN, 2015, URL: https://cds.cern.ch/record/2048202 (cit. on p. 32).

[53] ATLAS collaboration, *Expected performance of missing transverse momentum reconstruction for the ATLAS detector at $\sqrt{s}$ = 13 TeV*, tech. rep. ATL-PHYS-PUB-2015-023, CERN, 2015, URL: http://cds.cern.ch/record/2037700 (cit. on p. 32).

[54] ATLAS collaboration, *Luminosity determination in pp collisions at $\sqrt{s}$ = 8 TeV using the ATLAS detector at the LHC*, Eur. Phys. J. **C76** (2016) 653, arXiv: 1608.03953 [hep-ex] (cit. on p. 32).

[55] ATLAS collaboration, *Measurements of the production cross section of a Z boson in association with jets in pp collisions at $\sqrt{s}$ = 13 TeV with the ATLAS detector*, Eur. Phys. J. **C77** (2017) 361, arXiv: 1702.05725 [hep-ex] (cit. on p. 32).

[56] M. Czakon and A. Mitov, *Top++: A Program for the Calculation of the Top-Pair Cross-Section at Hadron Colliders*, Comput. Phys. Commun. **185** (2014) 2930, arXiv: 1112.5675 [hep-ph] (cit. on p. 33).

[57] M. Botje et al., *The PDF4LHC Working Group Interim Recommendations*, (2011), arXiv: 1101.0538 [hep-ph] (cit. on p. 33).

[58] J. Alwall et al., *The automated computation of tree-level and next-to-leading order differential cross sections, and their matching to parton shower simulations*, JHEP **07** (2014) 079, arXiv: 1405.0301 [hep-ph] (cit. on p. 33).

[59] ATLAS collaboration, *HistFitter: A software framework for statistical data analysis*, http://histfitter.web.cern.ch/histfitter/, [Online; accessed 2017-09-01] (cit. on p. 33).

[60] G. Cowan et al., *Asymptotic formulae for likelihood-based tests of new physics*, Eur. Phys. J. **C71** (2011) 1554, [Erratum: Eur. Phys. J.C73,2501(2013)], arXiv: 1007.1727 [physics.data-an] (cit. on pp. 33, 34).

[61] M. Baak et al., *HistFitter software framework for statistical data analysis*, Eur. Phys. J. **C75** (2015) 153, arXiv: 1410.1280 [hep-ex] (cit. on p. 33).

[62] ATLAS collaboration, *Jet reconstruction and performance using particle flow with the ATLAS Detector*, Eur. Phys. J. **C77** (2017) 466, arXiv: 1703.10485 [hep-ex] (cit. on p. 47).

[63] T. Sumida, *Jet calibration studies in the ATLAS detector*, https://indico.cern.ch/event/164609/contributions/1416567/attachments/197569/277307/toshi_report11.pdf, [Online; accessed 2017-09-18] (cit. on p. 47).

[64] ATLAS collaboration, *Topological cell clustering in the ATLAS calorimeters and its performance in LHC Run 1*, Eur. Phys. J. **C77** (2017) 490, arXiv: 1603.02934 [hep-ex] (cit. on p. 47).

[65] F. Demartin et al., *Higgs production in association with a single top quark at the LHC*, Eur. Phys. J. **C75** (2015) 267, arXiv: 1504.00611 [hep-ph] (cit. on p. 50).

[66] M. Carena et al., *11.Status of Higgs boson physics*, http://pdg.lbl.gov/2016/reviews/rpp2016-rev-higgs-boson.pdf, [Online; accessed 2017-09-18], 2016 (cit. on p. 50).

[67] ATLAS collaboration, *CentralMC15ProductionList*, https://twiki.cern.ch/twiki/bin/viewauth/AtlasProtected/CentralMC15ProductionList, [Online; accessed 2017-10-02], 2015 (cit. on pp. 53, 54).

APPENDIX A

Further studies

In this appendix, possible future directions of the dilepton channel are introduced. First, different jet reconstruction methods are considered in an attempt to improve the upper limit calculated in Chapter 6. The mechanisms are introduced and three different reconstruction methods are compared. Afterwards a first extrapolation to the single top production in association with a Higgs boson is made. The goal is to assess if the study of tHq production would be possible, when investigating a larger data set and using similar analysis techniques.

A.1 Particle flow

Both the calorimeters and the tracking detectors make it possible to gain information concerning the momentum of charged particles. Accordingly, either detector type can be used to measure the momentum of charged constituents of jets; however, only the calorimeters allow for the reconstruction of neutral constituents of jets. In Run~1 of the LHC the vast majority of analyses at ATLAS used the topological clusters of the calorimeters for jet reconstruction [62]. When speaking about topological clusters, two different energy scales can be employed: the electromagnetic scale (EM) or the local cluster weighting scale (LCW). In the case of the electromagnetic scale (EMTopo) the set-up is calibrated so that for electromagnetic showers (see section 3.3.2) the energy measured in the calorimeters is accounted for correctly [63]. In order to correct the energy of the jets measured in the calorimeters, jet energy scale corrections are applied afterwards. In the case of the local cluster weighting scale (LCTopo) an additional calibration step on cluster level is included: a weight is assigned to account for different shower types and detector differences. Afterwards jet energy scale corrections are once again applied [64].

In addition to these two different methods, called EMTopo and LCTopo from now on, a third reconstruction method is available for ATLAS: particle flow (PFlow) [62]. Instead of considering only the calorimeter measurements for jet reconstruction, particle flow uses information from the tracking detectors and the calorimeters. This makes it possible to combine the advantages of the calorimeters, which allow the reconstruction of neutral objects and have a good energy resolution at high energies, with those of the tracking detectors. There are several advantages of the tracking detectors [62]. First of all it should be noted that the resolution of the tracking detectors for low energies is much better than that of the calorimeters. The tracking detectors also make the use of a lower energy threshold for the acceptance of jets possible. In addition, the tracker has a better angular resolution of single charged particles and a higher probability of recovering low p_{T} charged particles that are typically swept out of the jet cone. Finally vertex association can be determined with higher precision. In Run~2, when PFlow chose the topological clusters for reconstruction, the electromagnetic scale was used as input.

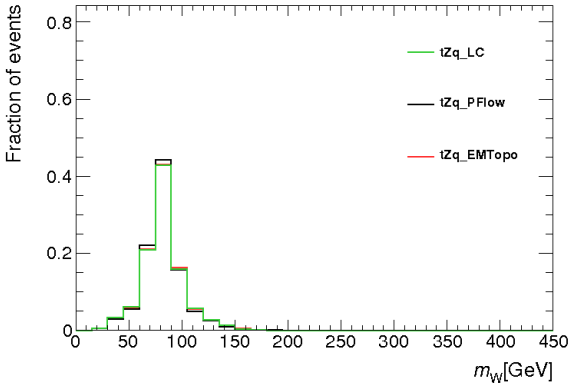

Figure A.1: Normalised shape comparison of the performance of the three different jet reconstruction methods for the reconstructed mass of the W boson.

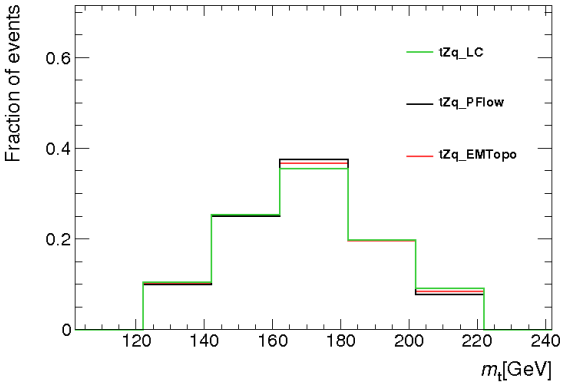

Figure A.2: Normalised shape comparison of the performance of the three different jet reconstruction methods for the reconstructed mass of the t-quark.

For the three different jet collections (EMTopo, LCTopo and PFlow) kinematic distributions and reconstructed quantities are compared both for the signal sample tZq as well as the background $t\bar{t}$ sample. The other samples were at the point at which this thesis was written not yet available. Compared to the main part of the analysis, slightly different Monte Carlo samples are used: For the signal samples, the generator used is still MadGraph, but with Pythia8 supplying the showering and hadronisation with A14 as the tune. For the PDFs, NNPDF23 at LO was used. In the case of $t\bar{t}$ the event generator is still PowhegBox, but instead of Pythia6, Pythia8 was used. For the PDFs NNPDF23 at LO were used and for the tune A14.

Due to better energy and angle resolution, the reconstruction using PFlow could lead to sharper peaks in the signal sample for the reconstructed particle masses involving jets, such as the W boson and the top quark. As observed in figures A.1 and A.2 the peaks of the W mass and the top mass are indeed slightly more pronounced though if one considers the statistical uncertainties, the effect is small (see figure A.3 and figure A.4). In addition one would expect better pile-up rejection for both the signal and the background sample. Since pile-up jets tend to have lower p_T one would accordingly expect a smaller number of entries for low p_T of the different jets. This effect was observed, but again does not lead to a significant impact (see figures A.5 and A.6). In order to draw a more general conclusion the cuts were lowered for these graphs: the number of possible jets and b-jets was left free. In addition the p_T cut for all jets was lowered to 30 GeV. Further jet distributions can be found in appendix D.

Despite some slight differences observed, none of them are significant enough to point towards a large effect on the training of the neural network. Accordingly the use of PFlow for jet reconstruction will not lead to significantly better signal/background separation. An improvement of the upper limit could be reached due to potentially better systematic uncertainties; however, these were not yet optimised for PFlow at the point at which this thesis was written.

A.2 Extrapolation studies for tHq production

Since its discovery, the study of the properties of the discovered Higgs boson is a subject of research (see chapter 2.1.1). The production of a top quark in association with a Higgs boson is a not yet discovered process (see figure 2.8). Accordingly it is of great interest to know if the production could be discovered with an analysis similar to the dilepton channel in tZq. An extrapolation study from the dilepton channel

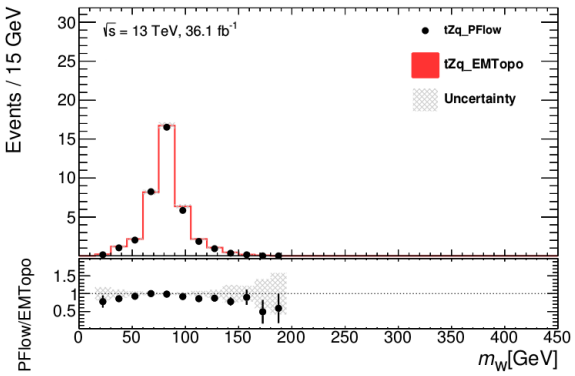

Figure A.3: PFlow to EMTopo comparison for the reconstructed mass of the W boson in the signal sample.

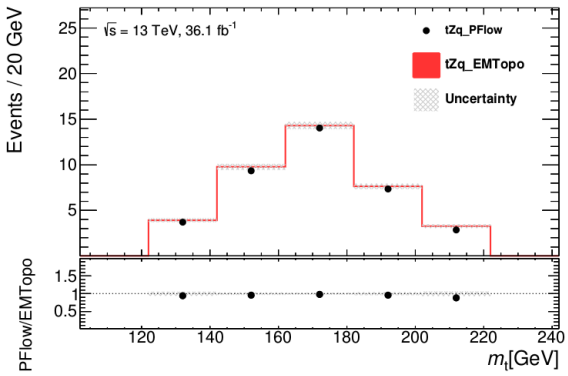

Figure A.4: PFlow to EMTopo comparison for the reconstructed mass of the t-quark in the signal sample.

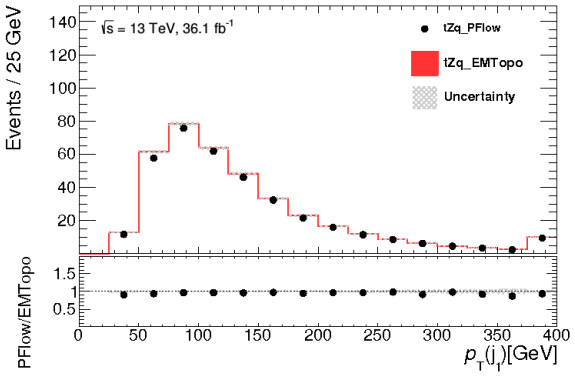

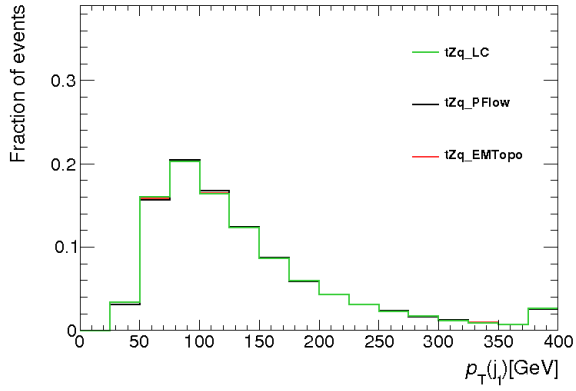

Figure A.5: Comparison of the three different jet reconstructions for the p_{T} of the leading jet in the signal sample.

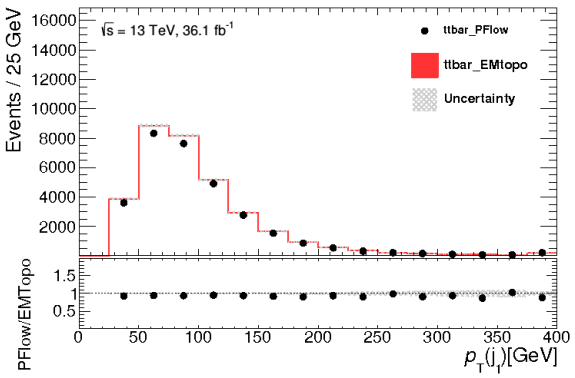

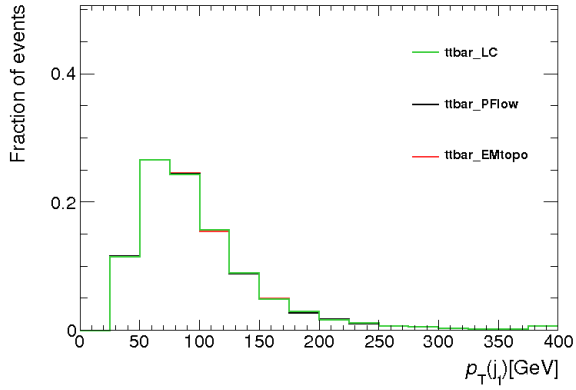

Figure A.6: Comparison of the three different jet reconstructions for the p_{T} of the leading jet in the $t\bar{t}$ sample.

of tZq can be done due to the similar possible final states of tHq and tZq. In tHq the W boson from the top quark would decay hadronically to two quarks ($q\bar{q}$) while the Higgs would decay into two photons. Accordingly similar to the dilepton tZq channel the final state would consist of four jets out of which one would be a b-jet. Instead of two leptons, two photons would be observed. In ATLAS their particle identification efficiency is similar to that of electrons and accordingly the decay of $tZq \to jjjbee$ can be treated as comparable to $tHq \to jjjb\gamma\gamma$. First, the number of theoretically predicted $tZq \to jjjbee$ will be calculated. Afterwards this value is compared to the number of Monte Carlo events remaining after all cuts are applied. A filtering efficiency can then be gained, which will be applied on the theoretical number of events for $tHq \to jjjb\gamma\gamma$. For the calculation of predicted number of tZq events the current integrated luminosity of 36.1 fb^{-1} and the cross section of $800\,\text{fb}^{+6.1}_{-7.4}\%$ were used (see section 4.3).

Since

$$N = L \cdot \sigma \tag{A.1}$$

with N being the number of particles, L the integrated luminosity and σ the cross section (see sectionf 2.1.3), it is possible to calculate the number of predicted tZq events:

$$N_{tZq,\,\text{pred.}} = (28.9^{+1.8}_{-2.1}) \cdot 10^3. \tag{A.2}$$

However not all of the produced tZq decay through the dileptonic channel. The branching ratios, $B_{2l} = \dfrac{\Gamma_{2l}}{\Gamma_{\text{tot}}}$, for the top decaying hadronically and the Z boson into two electrons are [6]:

$$B(t \to bq\bar{b}) = (66.5 \pm 1.4)\% \tag{A.3}$$

$$B(Z \to e^+e^-) = (3.363 \pm 0.004)\%. \tag{A.4}$$

This leads to a combined branching ratio of

$$B(tZ \to bq\bar{q}e^+e^-) = B(t \to bq\bar{b}) \cdot B(Z \to e^+e^-) = (2.24 \pm 0.05)\%. \tag{A.5}$$

Combining this with the number of predicted tZq events gives a total number of predicted events in the dilepton channel:

$$N^{2l}_{tZq,\,\text{pred.}} = 647^{+43}_{-49}. \tag{A.6}$$

Out of the 40.2 ± 0.7 weighted events observed after the cuts in table 5.2 only $N^{2l}_{tZq,\,\text{obs.}} = 17.1 \pm 0.5$ events have an electron pair for the two leptons. Accordingly the ratio of observed and predicted events is:

$$E_{tZq} = \frac{N^{2l}_{tZq,\,\text{obs.}}}{N^{2l}_{tZq,\,\text{pred.}}} = (2.64^{+0.19}_{-0.21})\%. \tag{A.7}$$

Applying this ratio on the predicted number of $tHq \to jjjb\gamma\gamma$ events will give an estimate of how many events can be expected to remain after cuts were applied. To calculate the number of predicted events the total integrated luminosity expected at the end of 2017 is used. It is 100 fb^{-1}. Together with the cross section $\sigma(tH + t\bar{H}) = (72.6 \pm 13.2)$ fb [65] this leads to $N_{tH,\,\text{pred.}} \approx 7200 \pm 1300$. The branching ratios of a Higgs boson decaying into two photons and the top quark decaying hadroncially are ([66] and [6]):

$$B(H \to \gamma\gamma) = 2.27 \cdot 10^{-3} \pm 5\% \tag{A.8}$$

$$B(t \to q\bar{q}b) = (66.5 \pm 1.4)\% \tag{A.9}$$

$$\Rightarrow B(Ht \to \gamma\gamma q\bar{q}b) = B(H \to \gamma\gamma) \cdot B(t \to q\bar{q}b) = (151 \pm 8) \cdot 10^{-5}. \tag{A.10}$$

This leads to 10.87 ± 0.57 events at $100\,\mathrm{fb}^{-1}$ being predicted for $tH \to \gamma\gamma q\bar{q}b$. Applying the ratio calculated above finally gives:

$$N^{2\gamma}_{tHq,\,\text{expected obs.,}} = E_{tZq} \cdot N^{2\gamma}_{tHq,\,\text{pred.,}} = 0.29^{+0.02}_{-0.03}. \tag{A.11}$$

One can conclude that using a similar set of cuts and $100\,\mathrm{fb}^{-1}$ of integrated luminosity would leave less than one event in the signal sample after selection. Accordingly this channel does not look promising for setting constraints on the tHq production cross-section. It would be advisable to consider other interesting decay modes for a possible cross-section measurement.

APPENDIX B

Additional information concerning the Monte Carlo samples

sample	generator	PDFs	shower, hadr.	order, tune
tZq	MadGraph 5.2.2	CTEQ6L1	Pythia 6	LO, Perugia 2012
Z+jets	Sherpa 2.2.1	nnpdf3.0	Sherpa 2.2.1	NNLO
$t\bar{t}$	Powheg-Box	CT10	Pythia 6	NLO, CT10
Wt	Powheg-Box	CT10	Pythia 6	NLO, CT10
tWZ	MadGraph 5_aMC@NLO	textscnnpdf3.0	Pythia 8	NLO, A14
WW, WZ, ZZ	Sherpa 2.1.1	CT10	Sherpa 2.1.1	LO
$t\bar{t}+W$	MadGraph 5_aMC@NLO 2.2.2	nnpdf2.3	Pythia 8	LO, A14
$t\bar{t}+Z$, $t\bar{t}+H$	MadGraph 5_aMC@NLO 2.2.3	nnpdf2.3	Pythia 8	LO, A14

Table B.1: Summary of the different Monte Carlo samples used in this analysis.

Table B.2: Overview of the signal and background simulated datasets [67].

Process	Sample ID	Generator	σ[pb]	k-factor	N-generated
tZq	410050	AMCNLO	0.240	1.00	996 849
$t\bar{t}$	410000	PowPy6Ev−P2012−ttbar−hdamp172p5−l	378	1.19	49 381 700
Wt	410015	PowPy6Ev−P2012−Wt−t−dil	3.58	1.05	992 885
	410016	PowPy6Ev−P2012−Wt−tbar−dil	3.58	1.05	992 021
ttH	343365	aMcAtNloPy8Ev−A14−ttH125−dilep	0.0534	1.00	236 049
	343366	aMcAtNloPy8Ev−A14−ttH125−sl	0.223	1.00	2 242 740
	343367	aMcAtNloPy8Ev−A14−ttH125−allhad	0.231	1.00	2 078 060
ttV	410066	MG5Py8Ev−A14−ttW−Np0	0.177	1.32	1 986 130
	410067	MG5Py8Ev−A14−ttW−Np1	0.141	1.32	2 353 360
	410068	MG5Py8Ev−A14−ttW−Np2	0.137	1.32	1 283 210
	410111	MG5Py8Ev−A14−ttee−Np0	0.00882	1.51	288 384
	410112	MG5Py8Ev−A14−ttee−Np1	0.0144	1.51	336 879
	410113	MG5Py8Ev−A14−ttmumu−Np0	0.00884	1.51	294 864

Process	Sample ID	Generator	σ[pb]	k-factor	N-generated
	410114	MG5Py8Ev−A14−ttmumu−Np1	0.0144	1.51	339 471
	410115	MG5Py8Ev−A14−tttautau−Np0	0.00901	1.51	294 864
	410116	MG5Py8Ev−A14−tttautau−Np1	0.0146	1.51	338 239
tWZ	410215	aMcPy8−tWZ−DR	0.0156	1.00	88 000
Diboson	361600	PowPy8Ev−AZ−WWlvlv	10.6	1.00	10 618 800
	361601	PowPy8Ev−AZ−WZlvll−mll4	4.51	1.00	4 390 160
	361602	PowPy8Ev−AZ−WZlvvv−mll4	2.78	1.00	2 730 000
	361603	PowPy8Ev−AZ−ZZllll−mll4	1.27	1.00	1 247 280
	361604	PowPy8Ev−AZ−ZZvvll−mll4	0.923	1.00	184 938
	361606	PowPy8Ev−AZ−WWlvqq	44.2	1.00	132 220 000
	361607	PowPy8Ev−AZ−WZqqll−mll20	3.28	1.00	957 952
	361609	PowPy8Ev−AZ−WZlvqq−mqq20	10.1	1.00	7 952 530
	361610	PowPy8Ev−AZ−ZZqqll−mqq20mll20	2.27	1.00	227 380
	344422	Sherpa−llll−BFil	0.0564	0.91	496 605
	344423	Sherpa−llll−BVet	0.833	0.91	2 956 390
	344424	Sherpa−lllvSFMinus−BFil	0.0233	0.91	100 430
	344425	Sherpa−lllvSFMinus−BVet	0.439	0.91	450 613
	344426	Sherpa−lllvOFMinus−BFil	0.0462	0.91	100 406
	344427	Sherpa−lllvOFMinus−BVet	0.871	0.91	988 863
	344428	Sherpa−lllvSFPlus−BFil	0.0355	0.91	998 547
	344429	Sherpa−lllvSFPlus−BVet	0.638	0.91	591 542
	344430	Sherpa−lllvOFPlus−BFil	0.0725	0.91	100 939
	344431	Sherpa−lllvOFPlus−BVet	1.31	0.91	1 193 370
	361068	Sherpa−llvv	14.0	0.91	4 036 770

Table B.3: Overview of the Z+jets background simulated datasets [67].

Sample ID	Generator	σ[pb]	k-factor	N-generated
364100	Sherpa−221−Zmumu−PTV0−70−CVetoBVeto	1 630	0.98	7 982 000
364101	Sherpa−221−Zmumu−PTV0−70−CFilterBVeto	224	0.98	4 983 000
364102	Sherpa−221−Zmumu−PTV0−70−BFilter	127	0.98	7 984 000
364103	Sherpa−221−Zmumu−PTV70−140−CVetoBVeto	75.0	0.98	5 983 000
364104	Sherpa−221−Zmumu−PTV70−140−CFilterBVeto	20.3	0.98	1 996 800
364105	Sherpa−221−Zmumu−PTV70−140−BFilter	12.4	0.98	5 981 600
364106	Sherpa−221−Zmumu−PTV140−280−CVetoBVeto	24.3	0.98	5 000 000
364107	Sherpa−221−Zmumu−PTV140−280−CFilterBVeto	9.28	0.98	3 000 000
364108	Sherpa−221−Zmumu−PTV140−280−BFilter	5.83	0.98	12 499 900
364109	Sherpa−221−Zmumu−PTV280−500−CVetoBVeto	4.77	0.98	2 000 000
364110	Sherpa−221−Zmumu−PTV280−500−CFilterBVeto	2.27	0.98	999 600
364111	Sherpa−221−Zmumu−PTV280−500−BFilter	1.49	0.98	1 999 400
364112	Sherpa−221−Zmumu−PTV500−1000	1.79	0.98	2 996 500
364113	Sherpa−221−Zmumu−PTV1000−E−CMS	0.148	0.98	1 000 000
364114	Sherpa−221−Zee−PTV0−70−CVetoBVeto	1 630	0.98	8 000 000
364115	Sherpa−221−Zee−PTV0−70−CFilterBVeto	224	0.98	4 999 000
364116	Sherpa−221−Zee−PTV0−70−BFilter	126	0.98	7 995 600

Sample ID	Generator	σ[pb]	k-factor	N-generated
364117	Sherpa−221−Zee−PTV70−140−CVetoBVeto	76.3	0.98	5 997 000
364118	Sherpa−221−Zee−PTV70−140−CFilterBVeto	20.3	0.98	1 999 200
364119	Sherpa−221−Zee−PTV70−140−BFilter	12.6	0.98	5 970 000
364120	Sherpa−221−Zee−PTV140−280−CVetoBVeto	25.0	0.98	5 000 000
364121	Sherpa−221−Zee−PTV140−280−CFilterBVeto	9.37	0.98	3 000 000
364122	Sherpa−221−Zee−PTV140−280−BFilter	6.07	0.98	12 499 600
364123	Sherpa−221−Zee−PTV280−500−CVetoBVeto	4.87	0.98	1 999 800
364124	Sherpa−221−Zee−PTV280−500−CFilterBVeto	2.28	0.98	999 900
364125	Sherpa−221−Zee−PTV280−500−BFilter	1.49	0.98	1 999 850
364126	Sherpa−221−Zee−PTV500−1000	1.81	0.98	3 000 000
364127	Sherpa−221−Zee−PTV1000−E−CMS	0.149	0.98	1 000 000
364128	Sherpa−221−Ztautau−PTV0−70−CVetoBVeto	1 630	0.98	7 996 000
364129	Sherpa−221−Ztautau−PTV0−70−CFilterBVeto	224	0.98	4 999 000
364130	Sherpa−221−Ztautau−PTV0−70−BFilter	128	0.98	7 995 800
364131	Sherpa−221−Ztautau−PTV70−140−CVetoBVeto	76.0	0.98	5 998 500
364132	Sherpa−221−Ztautau−PTV70−140−CFilterBVeto	20.2	0.98	1 999 200
364133	Sherpa−221−Ztautau−PTV70−140−BFilter	12.3	0.98	5 999 550
364134	Sherpa−221−Ztautau−PTV140−280−CVetoBVeto	24.8	0.98	5 000 000
364135	Sherpa−221−Ztautau−PTV140−280−CFilterBVeto	9.33	0.98	3 000 000
364136	Sherpa−221−Ztautau−PTV140−280−BFilter	5.48	0.98	4 999 950
364137	Sherpa−221−Ztautau−PTV280−500−CVetoBVeto	4.79	0.98	2 000 000
364138	Sherpa−221−Ztautau−PTV280−500−CFilterBVeto	2.28	0.98	1 000 000
364139	Sherpa−221−Ztautau−PTV280−500−BFilter	1.50	0.98	1 999 950
364140	Sherpa−221−Ztautau−PTV500−1000	1.81	0.98	2 999 800
364141	Sherpa−221−Ztautau−PTV1000−E−CMS	0.148	0.98	1 000 000

APPENDIX C

Distributions after event selection

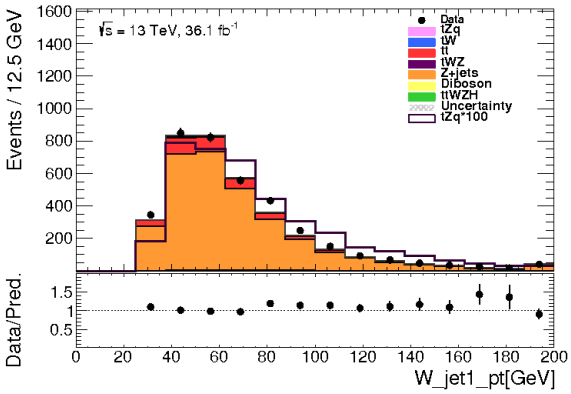

Figure C.1: Distribution of the p_T of the W-jet with the higher p_T after the event selection.

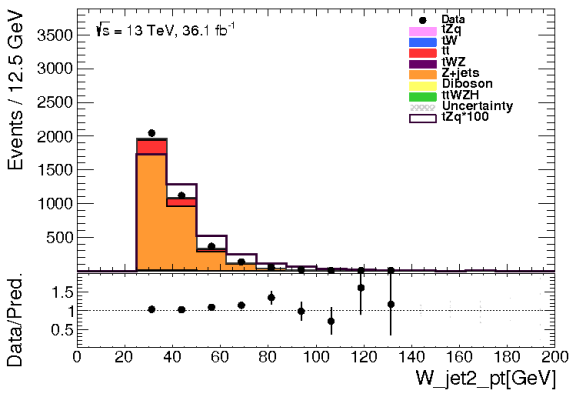

Figure C.2: Distribution of the p_T of the W-jet with the lower p_T after the event selection.

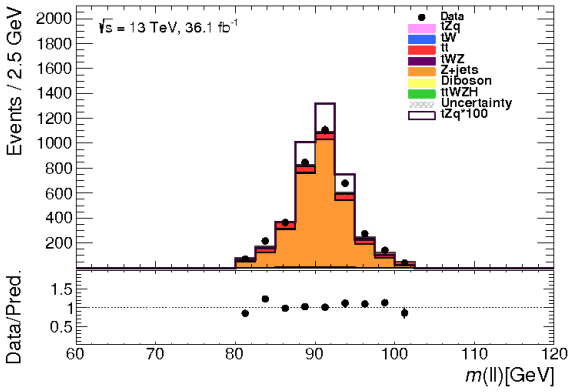

Figure C.3: Distribution of the reconstructed invariant mass of the Z-boson after the event selection.

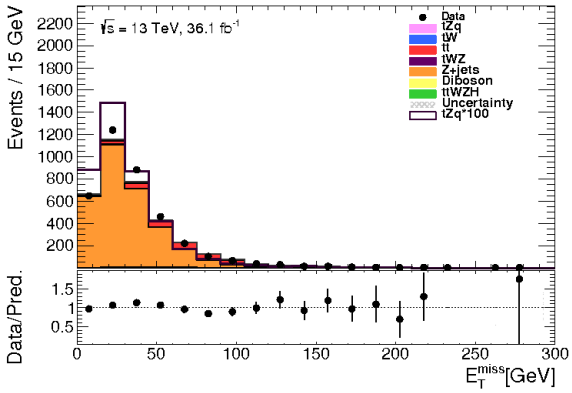

Figure C.4: Distribution of the missing transverse energy after the event selection.

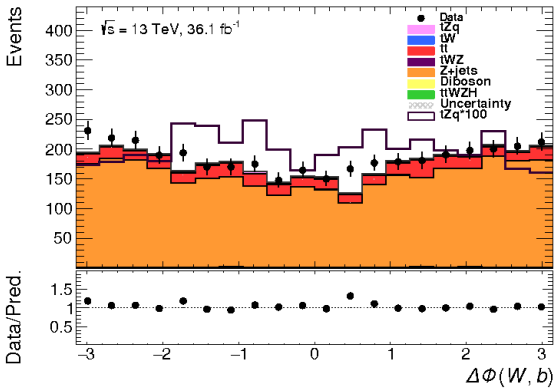

Figure C.5: Distribution of $\Delta\phi_{W,b}$ after the event selection.

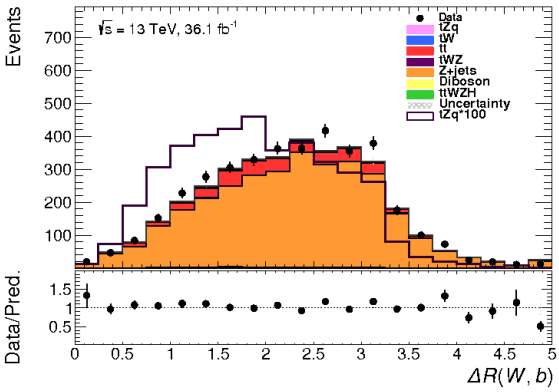

Figure C.6: Distribution of $\Delta R_{W,b}$ after the event selection.

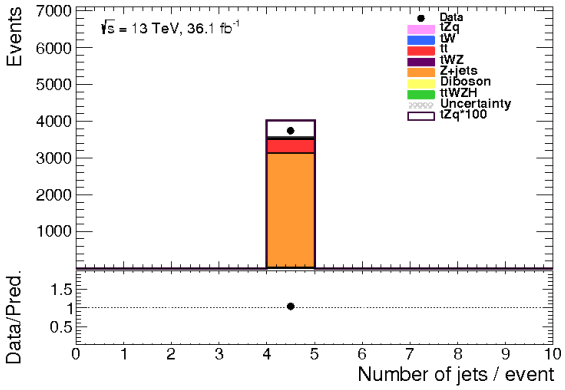

Figure C.7: Distribution of the number of jets after the event selection.

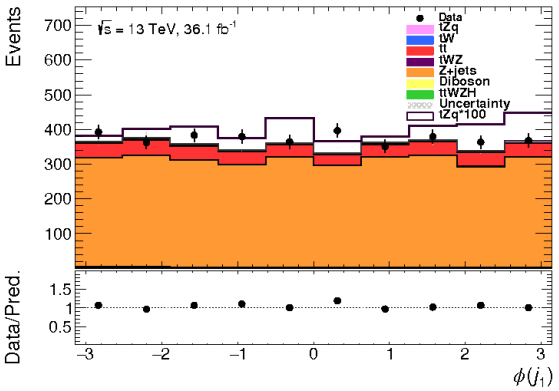

Figure C.8: Distribution of ϕ for the jet with the highest p_{T} after the event selection.

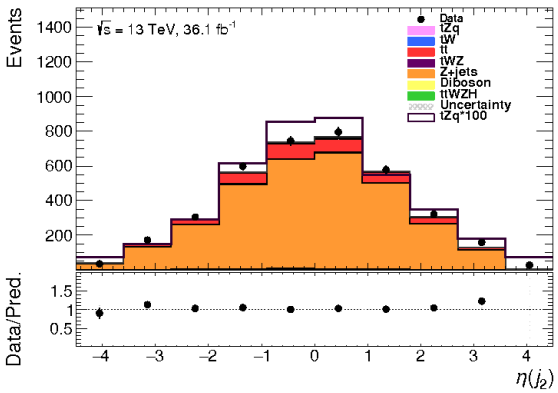

Figure C.9: Distribution of η for the jet with the second highest p_{T} after the event selection.

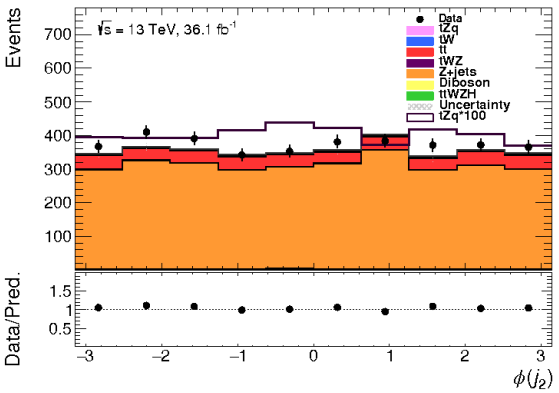

Figure C.10: Distribution of ϕ for the jet with the second highest p_{T} after the event selection.

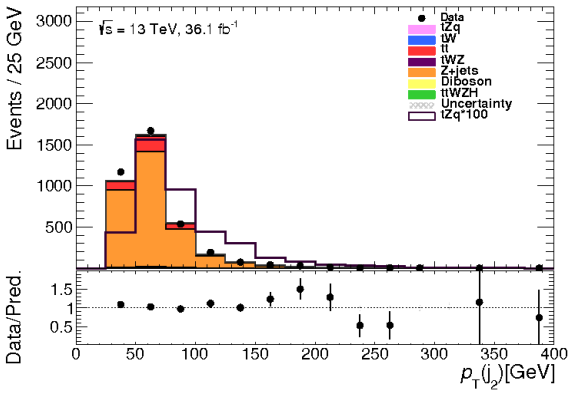

Figure C.11: Distribution of p_{T} for the jet with the second highest p_{T} after the event selection.

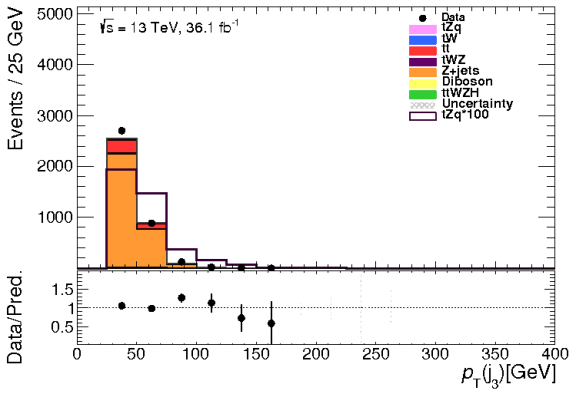

Figure C.12: Distribution of p_{T} for the jet with the third highest p_{T} after the event selection.

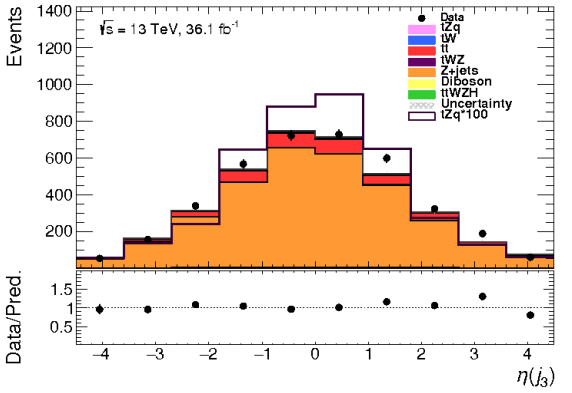

Figure C.13: Distribution of η for the jet with the third highest p_{T} after the event selection.

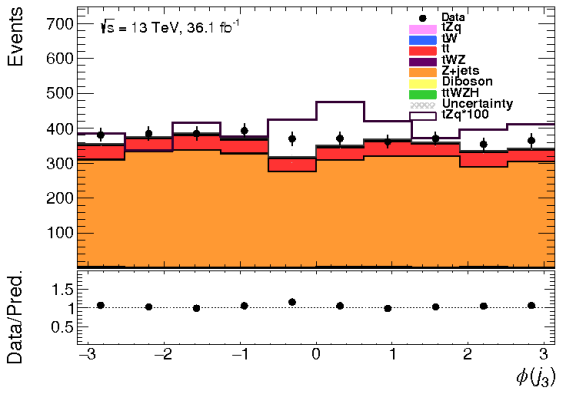

Figure C.14: Distribution of ϕ for the jet with the third highest p_{T} after the event selection.

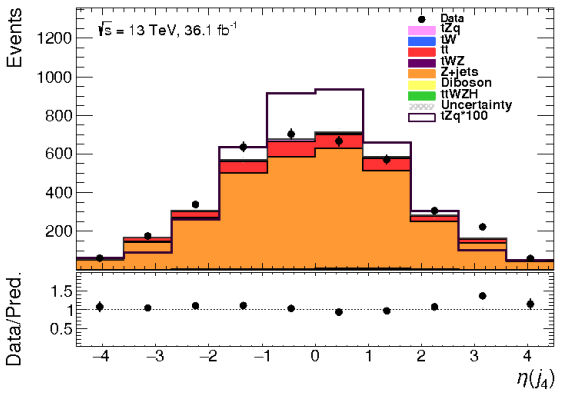

Figure C.15: Distribution of η for the jet with the lowest p_{T} after the event selection.

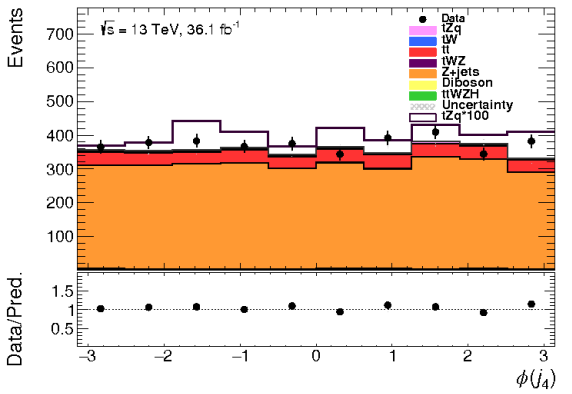

Figure C.16: Distribution of ϕ for the jet with the lowest p_{T} after the event selection.

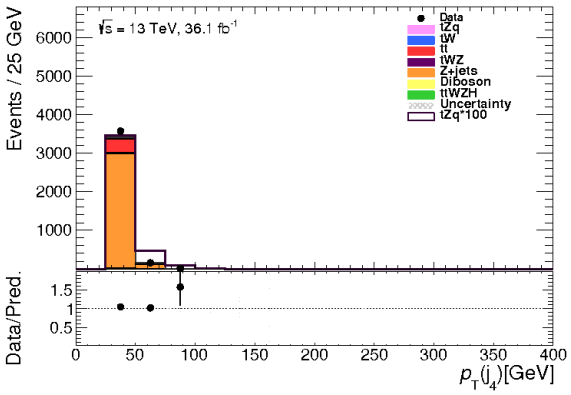

Figure C.17: Distribution of p_{T} for the jet with the lowest p_{T} after the event selection.

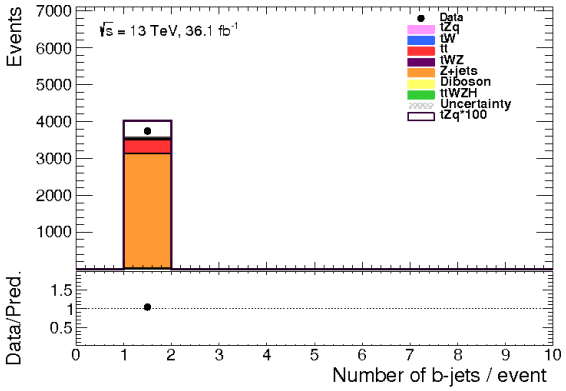

Figure C.18: Distribution of Number of b-jets after the event selection.

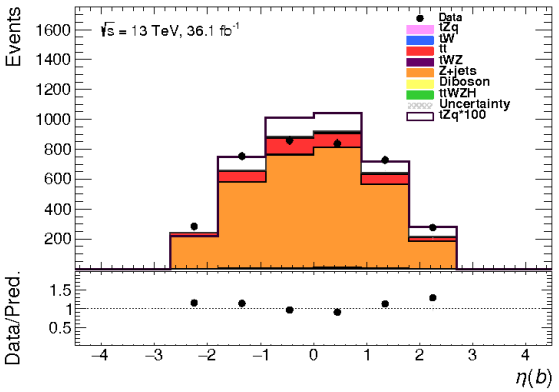

Figure C.19: Distribution of η for the b-tagged jet after the event selection.

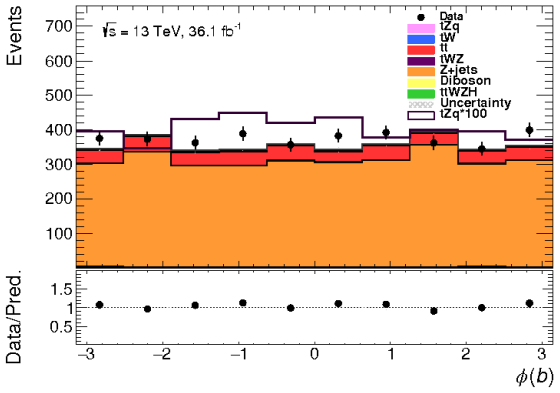

Figure C.20: Distribution of ϕ for the b-tagged jet after the event selection.

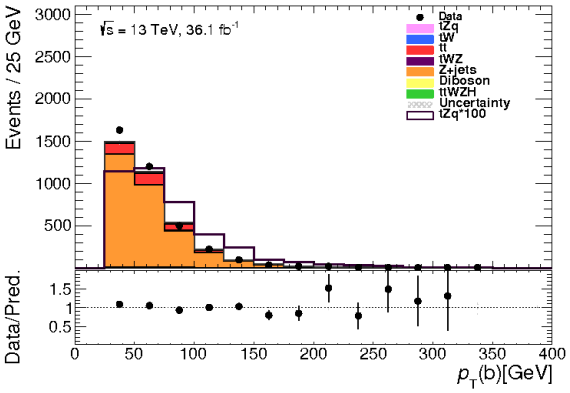

Figure C.21: Distribution of p_{T} for the b-tagged jet after the event selection.

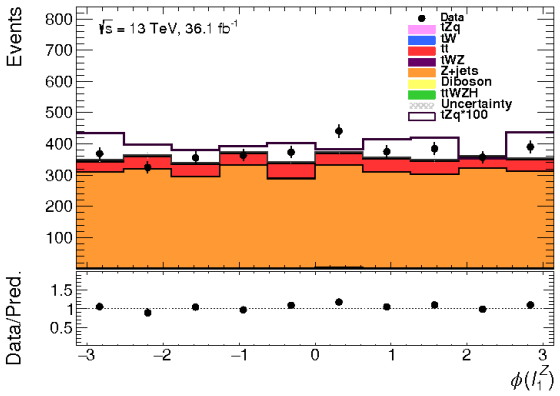

Figure C.22: Distribution of ϕ for the lepton with the higher p_{T} after event selection.

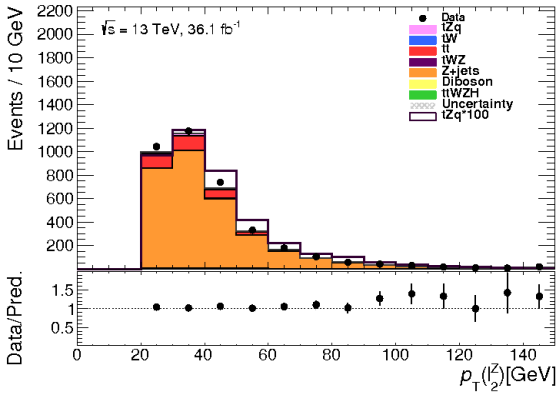

Figure C.23: Distribution of p_{T} for the lepton with the lower p_{T} after event selection.

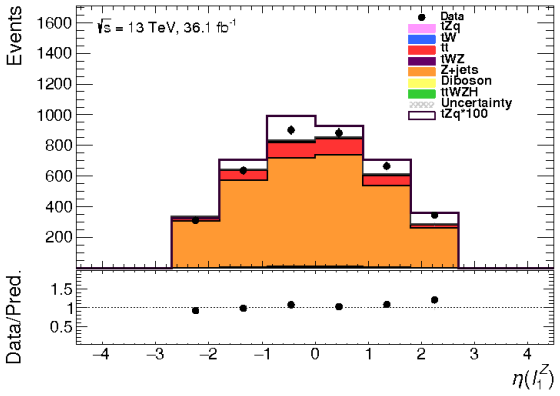

Figure C.24: Distribution of η for the lepton with the lower p_{T} after event selection.

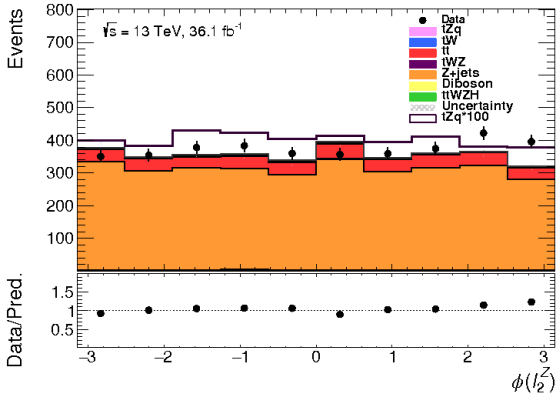

Figure C.25: Distribution ofϕ for the lepton with the lower p_{T} after event selection.

APPENDIX D

Distributions comparing jet collections

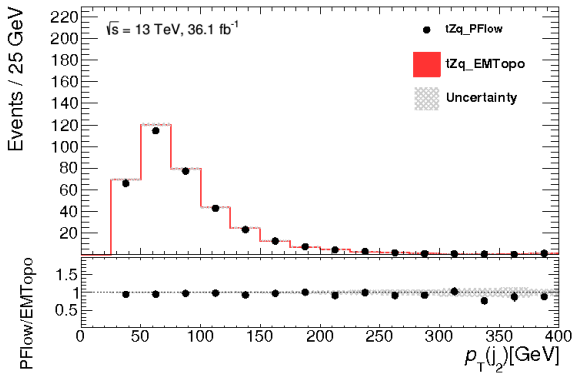

Figure D.1: PFlow to EMTopo comparison for the p_{T} of the second jet for the signal sample.

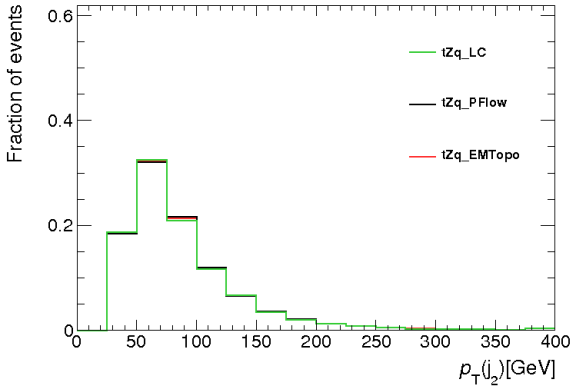

Figure D.2: Normalised shape comparison of three different jet reconstructions for the p_{T} of the second jet for the signal sample.

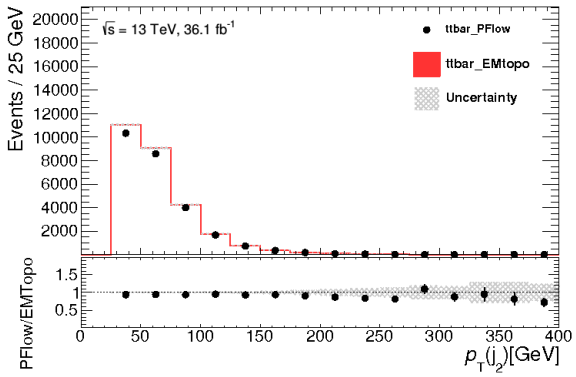

Figure D.3: PFlow to EMTopo comparison for the p_{T} of the second jet for the $t\bar{t}$ sample.

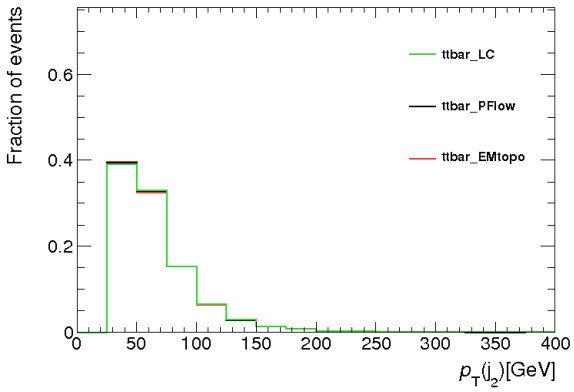

Figure D.4: Normalised shape comparison of the three different jet reconstructions for the p_{T} of the second jet for the $t\bar{t}$ sample.

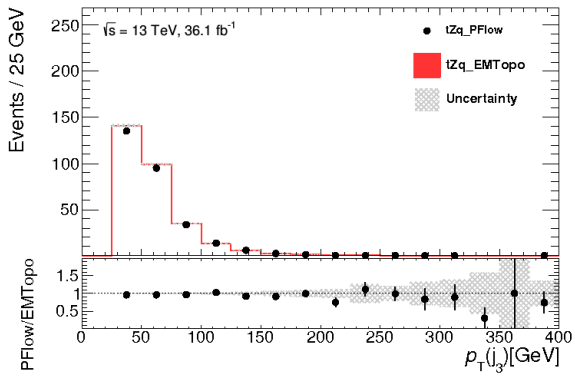

Figure D.5: PFlow to EMTopo comparison for the p_{T} of the third jet for the signal sample.

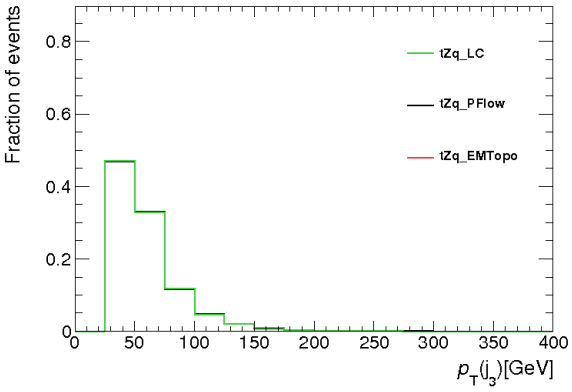

Figure D.6: Normalised shape comparison of the three different jet reconstructions for the p_{T} of the third jet for the signal sample.

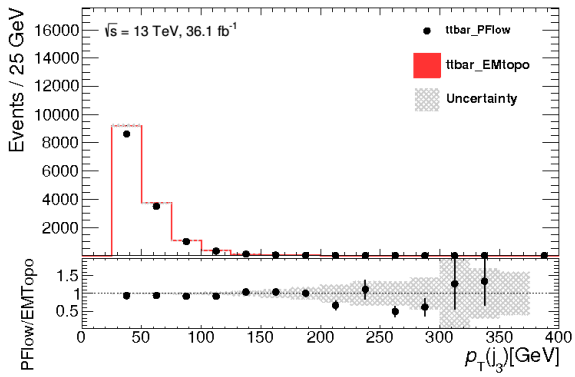

Figure D.7: PFlow to EMTopo comparison for the p_{T} of the third jet for the $t\bar{t}$ sample.

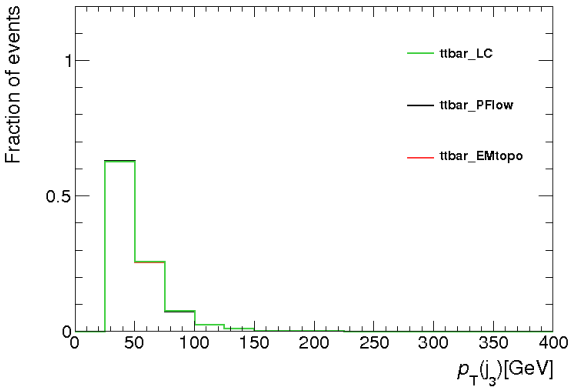

Figure D.8: Normalised shape comparison of the three different jet reconstructions for the p_{T} of the third jet for the $t\bar{t}$ sample.

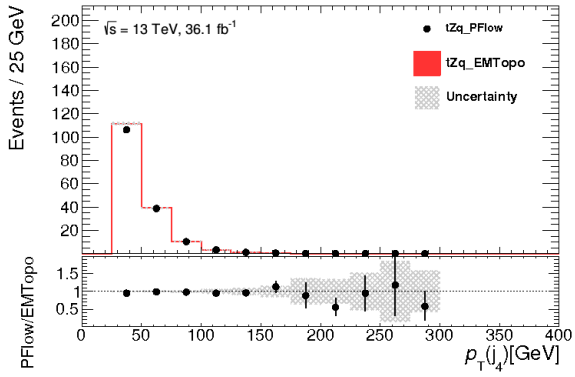

Figure D.9: PFlow to EMTopo comparison for the p_{T} of the fourth jet for the signal sample.

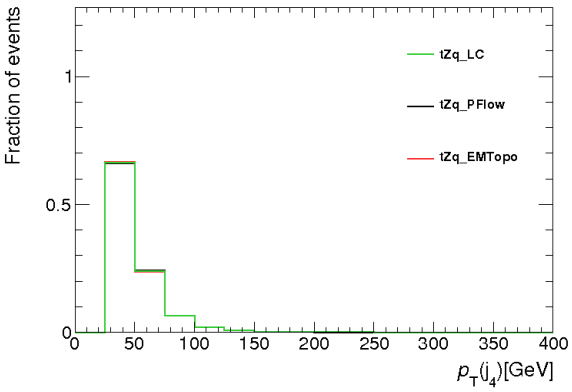

Figure D.10: Normalised shape comparison of the three different jet reconstructions for the p_{T} of the fourth jet for the signal sample.

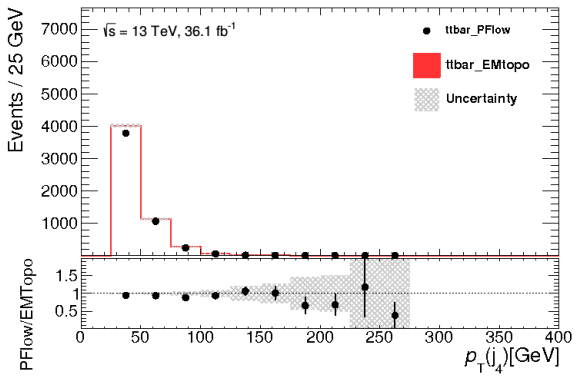

Figure D.11: PFlow to EMTopo comparison for the p_{T} of the fourth jet for the $t\bar{t}$ sample.

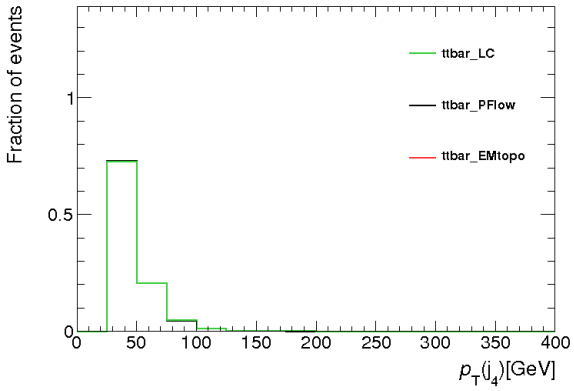

Figure D.12: Normalised shape comparison of the three different jet reconstructions for the p_{T} of the fourth jet for the $t\bar{t}$ sample.

List of Figures

List of Tables

Acknowledgements

In the course of the last year I greatly profited from the experience and knowledge of the Brock group. No matter how simple or difficult a question or problem was, there was always someone willing to take the time out of their busy schedule to explain matters or – if necessary – assist. For this I would like to thank all of the group: Professor Dr. Ian C. Brock, Dr. Regina Moles-Valls, Irina Cioarâ, Rui Zhang, Anjishnu Bandyopadhyay, Pienpen Seema, Ozan Arslan, Tanja Holm and Federico Guillermo Diaz Capriles. I would like to especially thank Professor Brock for giving me the chance to join the group. I would like to thank him for always being supportive and approachable. Despite the difference in experience, knowledge and age I always felt comfortable asking him for support and thanks to him I was able to go on several interesting schools and conferences. Another person who went far beyond what anyone could expect to assist me was Irina Cioarâ. I know that people claim that there are no stupid questions, but I am absolutely certain that I asked more than a few of them. I would like to thank her for being patient with me, for always being available and for teaching me how to approach a statistical analysis.

My year with the group certainly would not have been as much fun as it was without all of the discussions we had which were often completely unrelated with physics. I greatly enjoyed having the chance to get to know the opinions of so many people from such different backgrounds. Thank you for sharing your experiences with me.